PROF. AHMED EL HAWAT (Orcid ID : 0000-0002-5255-6823)

Article type : Original Manuscript

Early silicification of the Cyrenaican chert, Libya: The importance of moganite as a transitional silicon dioxide phase

Ahmed S. El-Hawat[1], Sue J. McLaren[2], Mohamed A. K. El-Ghali[3], and Simon J. Kemp[4]

[1]Department of Earth Sciences, University of Benghazi, Libya. ahmed.elhawat@uob.edu.ly

[2]School of Geography, Geology, and the Environment, Leicester University, LE1 7RH UK. sjm11@leicester.ac.uk

[3]Department of Earth Sciences and Earth Sciences Research Centre, Sultan Qaboos University, Oman. melghali@squ.edu.om

[4] British Geological Survey, Keyworth, Notts, NG12 5GG, UK. sjk@bgs.ac.uk

Associate Editor – Nicholas Tosca

Short Title – Diagenesis of chert from Cyrenaica NE, Libya

ABSTRACT

The Messinian lagoonal carbonate–evaporite sequence of Cyrenaica, north-east Libya, hosts: (i) opaline nodules in gypsiferous microbial-rich mudstone; (ii) nodules replacing poikilotopic gypsum cementing bioclastic carbonates; and (iii) bedded porcelanite with large lenticular gypsum pseudomorphs intercalated with recrystallized microbial mats. Optical microscopy, scanning

electron microscopy, backscattered electron images – secondary electron images, X-ray fluorescence, X-ray diffraction and cathodoluminescence techniques were employed to elucidate on the early stages of chert diagenesis and demonstrate the role of moganite in the formation of varieties of chalcedony during silicification. The opaline nodules composed of opal-A, exhibit shrinkage cracks lined by isopachous fibrous quartzine underlain by a thin birefringent zone. This suggests that quartzine may develop by crystallization and conversion of opal-A through a transitional moganite. The quartzine is followed by amorphous silica gel that converts into length-fast chalcedony. By contrast, lutecite evolved by silica replacement of gypsum through a transitional moganite phase, which forms an amorphous zone in apparent optical continuity with the fibrous lutecite; as moganite advances by pseudo-crystalline terminations controlled by the gypsum cleavage. In gypsified oyster shells, intercrystalline organic matter enveloping pseudomorphed shell microstructures enabled moganite nucleation that merges syntaxially around the gypsum crystal rim. The associated lutecite occurs as radial-fibrous beekite aggregates that are consistent with early shell silicification. The bedded porcelanite consists of opal-CT groundmass undergoing recrystallization and enclosing micro-cavities lined by quartzine. The associated pseudomorphs display phases of gypsum replacement by moganite and lutecite at the outer margin, followed by dissolution and cavity filling by quartz varieties in response to fluid flushing. In all cases, organic matter and microbes played a vital role in the silicification process.

Keywords: Chert, Cyrenaica, Libya, lutecite–quartzine, Messinian, moganite, opal, poikilotopic gypsum, pseudomorphs.

INTRODUCTION

The origin, diagenesis and mineralogy of chert are reviewed extensively by several researchers including Laschet (1984), Hasse (1989) and in Warren (2006). The relationship between length-slow chalcedony (quartzine and lutecite) and evaporites was studied and debated and given prominence by many authors (West, 1964, 1973; Folk & Pitman,1971; Chown & Elkins, 1974; Siedlicka, 1972, 1976; Tucker, 1976a, b; Milliken,1979; Geeslin & Chafetz,1982; Ulmer-Scholle, *et al.*, 1993; Chafetz & Zhong, 1998; Alonso-Zarza *et al.,* 2002; Khoriby, 2006). These studies enforced the notion that the occurrence of these minerals could be taken as evidence of an evaporite precursor. Evaporites and length-slow chalcedonic minerals are also found in deep marine pelagic sediments, and the latter in high Mg-calcite shells found in turbidites (Jacka, 1974; Keene, 1983, Scheffler *et al.,* 2014), indicating that length-slow silica minerals may also develop under non-evaporitic conditions.

Such debates initiated petrographic and mineralogical investigations of the length-slow silica minerals utilising modern optical microscopy, powder X-ray diffraction (XRD) analysis, transmission electron microscopy (TEM), scanning electron microscopy (SEM), infrared spectroscopy, and analytical chemical techniques by various authors. Heaney (1995), concluded that quartzine is not as reliable an indicator of vanished evaporites such as lutecite, because the crystallization of the former is influenced by the geochemical non-evaporitic diagenetic conditions, whereas the latter is always associated with evaporites unless it is in a volcanic environment. Significantly, this author (*ibid*) demonstrated that the diagenetic replacement of evaporites by lutecite takes place through moganite, a metastable silica polymorph phase. Moganite is structurally related to quartz, with a microstructure consisting of irregularly arranged length-slow fibres and bundles composed of platy aggregates (Miehe & Graetsch, 1992). Similarly, lutecite also consists of microcrystalline fibrous quartz aggregates, where fibres attain irregular shapes, V-shaped twinning and form bundles that may host some moganite in the structure (Nagasi *et al.*, 2013). In rocks, Bustillo (2001) reported the presence of moganite in chert nodules from Mg-rich continental clays. Nevertheless, Bustillo (2002) outlined the difficulty in recognizing moganite by optical means and emphasized the use of X-ray diffraction and refinement techniques as the best method for identification. In later research, it was concluded that moganite has a constant existence in all chalcedonic silica minerals regardless of their origin, depositional association or diagenetic environment (Bustillo *et al.*, 2012).

The Cyrenaican chert being of a relatively young age, closely associated with crystalline gypsum and microbial deposits, and subaerially exposed since the Messinian, offers an opportunity to study the early stages of silica diagenesis. In utilising optical microscopy, SEM and various geochemical methods, it is possible to trace and document the details of chert diagenetic events and timing that led to the development of different varieties of silica phases, where moganite plays a transitional role in mineral replacement and conversion.

Chert nomenclature

The SiO_2 mineral and textural phases that are recognized in the Cyrenaican chert and discussed in this work are previously reviewed by Laschet (1984), as well as others. These are briefly reviewed.

Opal – hydrous amorphous SiO_2 mineral varieties include: (i) opal-AG, colourless cavity-filling silica-gel, isotropic, contains trapped fluid inclusions; (ii) opal-A, khaki, waxy, breaks easily to conchoidal fracture, isotropic, replaces gypsiferous muddy microbial-rich sediments; (iii) opal-CT, milky-white, hard, breaks with smooth conchoidal surfaces and sharp edges, constitute nodules and thin beds with dewatering cracks.

Lepisphere – microphysical metastable aggregates of plate-shaped cristobalite–tridymite crystals of opal-CT.

Chalcedony – colourless, cavity-filling, radiating fibres with parallel length-fast extinction, negative elongation normal to c-axis.

Quartzine – fibrous, brownish with inclusions, length-slow extinction parallel to the c-axis, positive elongation.

Moganite – colourless, amorphous consists of platy fibrous quartz aggregate microstructure exhibiting length-slow brush or unit extinction.

Lutecite – colourless, fibrous length-slow, positive elongation with 30^o oblique extinction from the c-axis, fibres composed of porous, stacked platy quartz aggregates attain a 'Weetabix' texture.

Zoned quartz – brownish, cavity filling, length-slow fan-shaped crystals with zonation bands of fluid inclusions.

Megaquartz – cavity filling prismatic crystals with euhedral termination, equant to elongated grains larger than 35 μm.

Microcrystalline quartz – equant grains with vague outline commonly form low undulose birefringent aggregates, 20 μm to 5 μm or smaller.

Porcelanite – milky-white microbial-rich chert beds consist of opal-CT with minor amounts of opal-A, conchoidal fracture and shrinkage cracks.
Beekites or 'orbicules' – lozenge-shape texture with concentric multistage fibrous lutecite.
Spherules – rounded 10 to 50 μm in diameter with radial micro-fibrous nucleation of chalcedony minerals around coccoid bacteria.

GEOLOGICAL SETTING

The Miocene sequence exposed on the northern margin of Al Jabal al Akhdar inversion anticlinorium of Cyrenaica, north-east Libya (Fig. 1A), is a shallowing-up carbonate–evaporite succession referred to as Ar Rajmah Group (El Hawat *et al.,* 2004; Amrouni, 2015, 2016a). The Ar Rajmah Group is divided into two stratigraphic units separated by a major unconformity forming the Middle–Late Miocene boundary (El Hawat & Salem, 1987). The lower unit of the sequence consists of open shallow marine reefal and bioclastic carbonates of the Benghazi Formation (Langhian–Serravallian), overlain by the Tortonian–Messinian Wadi al Qattarah Formation (Fig. 1B). The chert investigated in this study and the ages of the associated carbonates and evaporites are confirmed as Messinian (5.34–5.71 Ma) by $^{87}Sr/^{86}Sr$ isotope data (Shaltami, *et al.*, 2018). The Messinian succession in northern Cyrenaica was never buried, because the region was subjected to post-Messinian tectonic uplift, erosion and karstification (El Hawat *et al.,* 2004).

The Wadi al Qattarah Formation consists of a prograding cross-bedded oolitic–oncoidal shoal facies overlain by restricted lagoonal carbonates and evaporites (Fig. 1B). These are composed of salina pond/lake gypsum, and muddy carbonate flats associated with back shoal shell bioaccumulation and grainy deposits (Fig. 1C). These facies pass laterally to the south into siliciclastic deltaic deposits fed by channels that issued from the adjacent Sirt rift complex (El Hawat 1980; El-Hawat, & Salem, 1987). The coarse-grained bioclastic facies were deposited in the lagoonal area during storm events (El Qot *et al.*, 2017). They consist of a reworked porous mixture of lithoclasts, ooids, oysters, shell debris, oncoids and other microbial debris found floating in the muddy or grainy matrix. These are locally cemented by poikilotopic gypsum crystals that enclosed the grain framework and occluded the intergranular and mouldic pore spaces. Chert nodules used in this study are found replacing sediments and cement in these deposits.

The salina pond deposits consist of laminated gypsiferous calcareous clay and chalk that in places may contain ostracod, dwarf molluscan shells and rare fish bones. South of the study area, gypsum deposits occur in thin discontinuous disturbed lenses exhibiting dissolution features and contamination by siliciclastic sediments that inhibited crystal growth. To the north and away from the siliciclastic source, giant crystalline selenite occurs in a series of vertically stacked lens-shaped bodies of different sizes; some are up to 200 m long by 150 m wide and about 15 m thick. These appear to occupy inherited structurally controlled depressions of the anticlinorium. Selenite crystals are swallow-tail twinned, vertically oriented with their apices pointed downward, being seeded in microbial gypsarenite at the base. These are arranged in centimetre to metre-scale beds attaining an upward increase in crystal size. Crystals grew subaqueously upward, competing for space laterally and reaching up to 3 m or more in height. These crystals are in optical continuity, taking the appearance of columnar structure in the field (Fig. 2A). These long crystals are interrupted by multiple internal dissolution surfaces and microbial inclusion (Fig. 2B and C), indicating cyclic salina water dilution followed by crystal growth (El Hawat, 1980). Sulphur isotope analysis data of nine stratigraphically distributed samples from the associated gypsum body provided $\delta^{34}S$ values of 23.3 to 23.7‰ with an average $\delta^{34}S$ of 23.3‰ (±0.2‰). The porcelanite chert with pseudomorphs and associated microbial beds are found a few decimetres above the selenite bodies (Figs 1C and 2A).

The muddy deposits are laminated, peloidal and chalky, and consist of gypsiferous lime mudstone and calcareous clay. The clays are dominated by montmorillonite and traces of mixed layer montmorillonite–chlorite minerals in the area associated with siliciclastics (Cesarano *et al.,* 2018). The exposed mudstone bedding surfaces exhibit occasional Cerithiidae gastropod trails, in addition to crinkly microbial surfaces and polygonal desiccation cracks suggesting alternation of wet and dry episodes during sedimentation. Mudstone beds are associated with laminated beds that may evolve locally into microbial mats and stromatolites are up to 1 m thick. Some microbial beds are altered by meteoric water diagenesis into porous coarse sparry calcite, often inter-bedded with porcellaneous chert layers that contain large pseudomorphs after lenticular gypsum. Thick stromatolitic build-ups may host large chert nodules (Fig. 2D) and gypsum, which when dissolved cause beds to collapse into brecciated rubble. Other beds exhibit chaotic soft-sediment deformation of tepee structures capped by gypsum cemented bioclastic deposits with chert nodules that extend for some distance along the outcrop (Fig. 2E).

METHODS

For this study, integrated standard petrographic techniques by optical and scanning electron microscopy (SEM) and cathodoluminescence (CL) were employed to establish the types, texture, composition and timing of diagenetic events during silicification. The nomenclature of Folk & Weaver (1952) is used to describe fabrics characteristic of silica replacement. Freshly broken pieces of chert were coated by vaporised gold and surfaces examined by JEOL SEM JSM-36 with Kevex Mx 7000 system (JEOL Limited, Tokyo, Japan). In preparation for the petrographic examination, thin sections were cold-mounted to avoid alteration of gypsum crystallinity. In addition, thin sections are generally ground larger than the standard thickness due to the contrasting hardness between gypsum and the silica minerals. As a result, the interference colours of minerals are higher than usual.

To support the petrographic work, geochemical analysis included X-ray diffraction phase quantification of selected samples using the Rietveld refinement technique (e.g. Snyder & Bish, 1989), at the British Geological Survey. Isolated sub-samples were hand-crushed in a pestle and mortar and then ball-milled. In order to provide a finer and uniform particle-size for powder XRD analysis, a 4.5 g portion of the ball-milled sample was micronized under deionised water for 10 minutes with 10% (0.5 g) corundum (American Elements – PN:AL-OY-03-P) and dried at 55°C. The addition of an internal standard allows the validation of quantification results and also the detection of any amorphous species present in the samples. Corundum was selected because its principal XRD peaks are suitably remote from those produced by most of the phases present in the samples. The micronized powders were front-loaded into standard, stainless steel sample holders for analysis. Additional XRD analyses were carried out using a Malvern Panalytical X'Pert Pro series diffractometer equipped with a cobalt-target tube, X'Celerator detector and operated at 45kV and 40mA (Malvern Panalytical, Malvern, UK). The powder mounts were scanned from 4.5 to 85^{o}2 at 2.06^{o}2/minute.

Diffraction data were analysed using Malvern Panalytical X'Pert HighScore Plus version 4.8 software coupled to the latest version of the International Centre for Diffraction Data (ICDD) database. Further powder X-ray diffraction (XRD) conducted in Oman used the PANalytical X'Pert Pro X-ray diffraction system; wavelength dispersive X-ray spectrometry (XRF) Axios^{mAX} model, used for bulk chemical analysis of rocks, and scanning electron microscope (SEM) compo

equipped used for high-resolution images, energy dispersive X-ray for spot chemical analysis (EDS), and backscatter image analysis (BSI).

RESULTS

The opaline nodules

The opaline nodules occur in soft, slightly moist gypsiferous microbial-rich clayey mudstone beds. These are found in a sequence with bioclastic carbonates, microbial mats, gypsum beds and tepee structures. The mudstone beds also host some soft ovoid gypsum nodules ranging from 5 mm to 6 cm in diameter composed of an amalgamation of minute lenticular crystals and a variable amount of the host sediments. The enclosing mudstone matrix consists of floating minute lens-shaped gypsum crystals, microbial pellets, small oncoids and occasional dwarf shell moulds (Fig. 3A). A few of the gypsum nodules are found partially encased by silica and remain open on one side. Their outer opaline shell is khaki coloured, waxy and 1 to 2 cm thick on average, while their gypsum core exhibits some degree of dissolution forming partial cavities.

Well-formed oval-shaped completely silicified opaline nodules are up to 5 cm in diameter, khaki to yellowish-grey (5Y7/2) in colour, waxy in feel and appearance. These are not fully hardened and easily broken, exhibiting a smooth conchoidal fracture surface. These nodules are found a few centimetres deep in the mudstone beds, and still contain gypsum and sediments undergoing replacement by silica with relatively high-water content. In thin sections, birefringent minute lenticular gypsum crystals are either separate or merge in paint-brush stroke clusters as they lose their outlines in a dark matrix (Fig. 3B). Although nodules were not X-ray analysed, they are presumed to be composed of immature opal-A. However, on exposed weathered surfaces, nodules are hardened, turning milky white (N9) in colour, and exhibit dehydration shrinkage cracks 0.5 to 3.0 mm wide. In thin sections, the nodule groundmass consists mostly of isotropic, amorphous silica, attaining more than 80wt% SiO_2 in composition (Table 1). The loss of moisture due to subaerial exposure and evaporation induced silica crystallization (Laschet, 1984). X-ray diffraction analysis indicates that these nodules are composed of tridymite, and some quartz in addition to gypsum. Cristobalite was not identified in the analysed sample, suggesting an early incomplete conversion to opal-CT. Silicified carbonate and clay particles, moulds of dwarf shells, microbial grains and oncoids are also found in these nodules. Spot SEM–SEI–BSI analysis of

silicified microbial filaments composing the silicified oncoids indicate 31 to 49 wt% carbon content (Fig. 3C; Table 2).

Close SEM examination of the walls of the nodule dehydration cracks shows a botryoidal, crenulated surface with needle fibre terminations (Fig. 3D). In thin sections, these cracks are lined by 0.1 to 1.5 mm thick isopachous fibrous crust of brownish rows of length-slow quartzine. This exhibits successive parallel growth lines consisting of dark inclusions that run across the length of the fibres and parallel to the crack wall. Some of the inclusions are large opaline slivers that appear to have been detached from the nodule wall, as fibres grew towards the central cavity of the crack (Fig. 3E). In some thin sections, the quartzine cavity lining is covered by an amorphous, translucent, isotropic, silica layer that, in places, may exhibit a serrated outer surface (Fig. 3E). This material fills the shrinkage crack central cavities and commonly encloses trapped fluid bubbles (Fig. 3F) that suggest rapid precipitation from supersaturated silica solution (Folk & Pittman, 1971; Laschet, 1984). This is interpreted as silica gel (opal-AG), that later crystallizes into fibrous length-fast chalcedony. Under normal light, the chalcedony is translucent and attains a radial-fibrous texture resting on the isopachous brown quartzine (Fig. 3G). Under high SEM resolution the chalcedony appears as radiating cone-shaped fibrous bundles, where fibres consist of stacked quartz crystallites. These crystallites are elongated perpendicular to the fibrous growth producing the characteristic optical length-fast vibration direction (Fig. 3H).

Significantly, some of the quartzine cavity linings are separated from the nodule's opaline wall by a narrow birefringent zone. Under crossed polars, this zone exhibits either length-slow wavy extinction, and in places goes into unit extinction as a single crystal around the cavity (Fig. 3F and G). It is interpreted as moganite that formed the transition in the replacement of opal by quartzine (Heaney, 1995), in a solid to solid conversion process (Laschet, 1984). Meanwhile, some shrinkage crack central cavities are filled by geopetal muddy sediments (Fig. 3G), length-fast silica spherules and quartz grains.

Chert nodules in gypsiferous bioclastic carbonates

Chert nodules are associated with gypsiferous coarse bioclastic lag and storm deposits forming laterally traceable layers along the outcrops (Fig. 2E). These rocks are composed of an ill-sorted mixture of molluscan shells and moulds of oyster shells with bored micritized microbial envelopes, lithoclasts, oncoids, ooids, microbial grains and pelletal mud matrix of various

proportions. Lithoclasts and complete shell size components have formed shelter cavities and preserved a good porosity framework in these rocks. This pore network created the space suitable for precipitation and growth of poikilotopic gypsum crystals from groundwater saturated by calcium sulphate ions. Gypsum crystals infilled pore spaces and enclosed the grain framework, and partly replaced some grains and matrix. Crystals are lenticular, up to 10 cm in diameter and about 3.5 to 4.0 cm across at the centre. Some of these crystals amalgamate in a different orientation to form a Desert Rose pattern inside the rock (Warren, 1991). In cross-section, associated chert nodules measure 5 to 15 cm long and 2 to 5 cm thick, and attain a dark grey colour at the core and light whitish colour in the margins (Fig. 4A). The colour contrast between the margin and the core is attributed to the degree of silicification of the rock components, as silicification advances against gypsum with a moganite front (Fig. 4C to E). The nodule outer surfaces are very rough, attaining an amoeboid appearance, as silica protuberances advance, and replace the carbonate grains, matrix and the gypsum cement poikiloblasts. This makes it difficult to extract clean nodules from the host sediments. When hammered, rocks tend to break preferentially along the prominent (010) cleavage surfaces of gypsum. In silicified muddy oolitic nodules where the pore spaces are not interconnected, gypsum pseudomorphs occur in isolated large lenticular crystals. Ooids in these nodules are replaced by opaline silica, and exhibit early deformation against the pseudomorphed gypsum (Fig. 4B).

Two distinctive interrelated modes of silicification of poikilotopic gypsum are observed in these chert nodules. The first is the direct replacement of pore-filling poikilotopic gypsum crystals by silica, and the other is the silicification of gypsified shells. In hypersaline sabkha and lagoonal environments, calcite and aragonitic shells are commonly susceptible to replacement by pseudomorphing of their internal microstructure by calcium sulphate (Bandel *et al.*, 1986). The chert nodules in these rocks attain less than 60 wt% SiO_2 content (Table 1). Standard X-ray analysis indicates that quartz is the dominant silica mineral in chert. However, application of XRD refinement techniques on selected samples confirms the presence of moganite and indicates that it constitutes up to 21.6 wt% of the sample (Table 3); taking into consideration that these analytical techniques may attain ±5 wt% error for samples where moganite concentration is between 20 wt% and 50 wt% (Kemp *et al.*, 2016).

Silicification of the poikilotopic gypsum cement

Optical method examination of the Cyrenaican chert suggests that, whereas opalization is favoured in the early silicification of nodules composed of minute gypsum crystals in muddy carbonate-rich sediments, lutecite is the preferred length-slow chalcedony mineral in the replacement of poikilotopic gypsum cement and pseudomorphs (Fig. 4B to D). As in the gypsum nodules, silicification of pore-filling gypsum poikiloblasts starts at the margin and proceeds inward towards the centre where lutecite occurs in two textural motifs. Silicification starts at the pore wall by forming 10 to 15 μm thick rims of crowded isopachous or radial-fibrous length-slow lutecite rosettes composed of curved aggregates, which occasionally enclose minute gypsum inclusions. It is followed inward by rows of straight, semi-parallel irregularly overlapping blades of fibrous lutecite texture that exhibit characteristic 30^{o} extinction (Fig. 4C and D). These two textural fabrics are separated by a narrow translucent, isotropic boundary observed in most of the examined thin sections. Under the high-resolution microscopy and SEM, lutecite blades are up to 100 μm long and 3.5 to 5.0 μm wide, exhibiting porous, platy crystallite texture (Fig. 5A). These are reported as microcrystalline quartz aggregates that contain up to 10 wt% moganite (Nagasi *et al.,* 2013).

Under normal light, lutecite fibre growth terminations form a 3 to 6 μm zone of zigzagged parallel lines (Fig. 4C and D). This zone forms an optical transition as it passes into 30 to 140 μm wide, amorphous translucent phase with a smooth surface texture. Under crossed polars, this latter phase exhibits a length-slow brush extinction pattern gradationally in tandem with the orientation of the lutecite fibres. It joins laterally and wraps around the lutecite in apparent syntaxial unit extinction at the boundary with the gypsum crystal (Fig. 4D). Under SEM examination of gold-coated, freshly broken surfaces, this mineral phase attains low relief felted or chevron textural patterns forming a well-defined contact with gypsum (Fig. 4E). The silica (SiO_2) – gypsum ($CaSO_4.2H_2O$) boundary is porous (Fig. 5A), and defined by pseudo-crystalline quartz terminations controlled by the gypsum cleavage planes, which appear to facilitate the molecular level solids exchange of gypsum by silica (Fig. 4C to E). This mineral phase is interpreted as moganite because it forms the conversion transition between the lutecite and gypsum (Miehe & Graetsch, 1992; Heaney, 1995). Although lutecite and moganite textures are optically recognizable in examined thin sections and by SEM, however, under higher resolution, both attain microstructures consisting of porous, flaky, stacked quartz aggregates forming what is referred to here as 'Weetabix' texture (Fig. 5A). It has

been established that lutecite microstructure hosts up to 10 wt% moganite (Nagasi *et al.* 2013), and it is possible to recognize moganite and quartz in the XRD spectrum, yet lutecite is not identified. However, other peaks in the spectrum suggest the presence of a quartz–moganite mix that may refer to lutecite (Fig. 9).

It is worth noting that the colour difference indicated between the nodule's core and its outer rim also corresponds to a contrast observed under the microscope. Whereas moganite forms a narrow zone at the silica–gypsum interface at the nodule's rim (Fig. 4C to E), it occurs in a relatively larger area in its core, as the poikilotopic gypsum cement is almost totally replaced by silica (Fig. 4F). Similar contrasts are reported by Bustillo (2001), where XRD analysis data suggests the presence of moganite in higher concentration in the chert nodule's core compared to that at its rim.

Silicification of gypsified shells

Microscopic examination of gypsified oysters and other shells indicates that they are pseudomorphs replaced by cloudy, brownish poikilotopic gypsum that has retained the original shell crystallite microstructure. The crystallite pseudomorphs are organized in semi-parallel lamellar patterns consisting of 30 μm wide rectilinear bundles exhibiting an internal herringbone micro-texture. These bundles are partially separated by microscopic translucent areas that used to be occupied the original intercrystallite organic matter. These are found to be zones of preferred SiO_2 nucleation in shells (Daley & Boyed, 1996; Butts, 2014). Under normal light examination, these narrow preferred silicification areas are found to spread into the surrounding gypsum forming smooth amorphous patches. These bold areas tend to merge and coalesce around the gypsum poikiloblasts periphery to form 80 to125 μm wide birefringent zones. Under crossed polars, these silicified areas exhibit unit extinction as a single crystal in syntaxial optical continuity corona (Fig. 5C and D).

Apart from the preservation of the original microbially bored micritized shell envelopes (Fig. 5B, E and F), and some faint ghosts of gypsum (010) cleavage, these smooth silicified areas do not retain evidence of the shell micro-structure. As for the lutecite–gypsum transition zone described earlier, these translucent silicified areas are interpreted as moganite (Heaney, 1995). However, these moganite zones are optically distinct from the hosting gypsum, as well as the adjacent

fibrous lutecite (Fig. 5C and D). The lutecite in this case occurs as single lozenges called 'beekites or orbicules' by some authors (Schmitt & Boyd, 1981; Elorza & Orue-Etxebarria, 1985; Mišík, 1995), and are usually surrounded by a moganite transitional halo. These beekites coalesce laterally in line following the original structural layering within the thick shell structure (Fig. 5D). Lozenges are 1 to 2 mm in size, consisting of a radial–fibrous lutecite texture exhibiting two phases of growth in optical continuity. In transmitted light, the early phase consists of zoned cloudy fibrous blades passing into a late phase of clear overgrowth that forms a distinctive serrated boundary against the moganite (Fig. 5C to E). The first phase may have been formed as an early replacement of the shell and the latter clear phase formed by the conversion of the moganite. Because most previous authors agree that intercrystalline organic matter makes calcite shells susceptible to silicification (Daley & Boyed, 1996; Butts, 2014), it is reasonable to assume that silicification may have, at least partially, preceded shell gypsification. However, it is an open question as to the timing of the Cyrenaican oyster shell silicification, because evidence is masked by later replacement by gypsum.

Porcelanite – microbial carbonate couplets and pseudomorphs

The bedded porcelanite alternates with recrystallized microbial carbonate layers forming 1.5 to 8.0 cm thick couplets. The porcelanite layers are in places covered by a paper-thin khaki green clay veneer between exhumed gypsum pseudomorphs on the bed surface (Fig. 6A). The clay may contain grains of minute detrital minerals, mica and show iron oxide staining. North of the study area, where the selenite gypsum bodies are well-developed, the porcelanite–carbonate couplets are interbedded in a succession of cross-bedded; gypsum cemented oncoidal packstone, and recrystallized partially silicified microbial mats and stromatolites (Figs 1C and 2D). In places, this succession is locally associated with chaotic evaporite solution-collapse breccia layers. To some extent, the Cyrenaican porcelanite–carbonate couplet units resemble the Ordovician Ribbon chert of Geeslin & Chavetz (1982).

The microbial carbonate layers

The boundary between the porcelanite and carbonate layers in the couplets is well-defined, wavy and curved as these layers are randomly traversed by displacive lenticular moulds and

pseudomorphs after gypsum (Fig. 6B). In hand-specimens, the carbonate layers exhibit lamination relics locally disrupted by the growth and dissolution of gypsum crystals, and during recrystallization of the host sediments. Sample X-ray analysis indicates the carbonate layers consist mainly of calcite with minor quartz content. Calcite crystals are equant, blocky, sometimes zoned, and mostly range between 10 μm and 20 μm in size, forming open porous textures, with some moulds also lined by calcite. The carbonate beds also enclose some silicified lenticular gypsum pseudomorphs with vague outlines, and white porous siliceous laminae and streaks (Fig. 6B). The pseudomorphs form siliceous masses preferentially filled by length-fast chalcedony, microcrystalline and megaquartz crystals, but with the noted absence of any length-slow chalcedonic minerals. The associated siliceous streaks consist mostly of opaline masses of lepispheres, where some appear to be in the process of etching into the calcite crystals in a dissolution–precipitation process and causing extensive corrosion (Fig. 6C). In places, calcite crystals are completely encased by opaline silica and in the process of being replaced by a delicate fibrous silica front (Fig. 6D).

Although the original microbial structure is preserved in thick stromatolite beds, it is mostly destroyed by gypsum dissolution and extensive recrystallization of the carbonates in the couplets. Optical and SEM observations of the siliceous laminae and streaks reveal rich fossilized microbial bacteria, (possible) filamentous fungal mats and degraded organic sheets (Fig. 6E and F). Spot SEM analysis of these filaments attains 20.5 wt% silica and up to 27.7 wt% carbon content (Table 2). Qualitative XRD methods detected the presence of moganite traces in the stromatolite samples; however, it was not significant enough to exceed beyond the error limit to quantify due to the overwhelming presence of calcite (Table 3). These fossil filamentous and microbial findings are consistent with those previously reported in dolomitized and silicified anhydrite nodules (Alonso-Zarza *et al.*, 2002) and ancient stromatolites (Perri & Tucker, 2007; Roemers-Oliveira *et al.*, 2015). The diagenesis and recrystallization of the microbial carbonate beds and their textural fabrics are analogues to the boxwork boundstone units described from the marginal deposits of the Holocene coastal salinas of southern Australia; where groundwater levels and chemistry fluctuate seasonally (Warren, 1982).

The porcelanite beds

The Cyrenaican porcelanite chert is white, hard and brittle, and tends to break in smooth conchoidal surfaces and sharp edges, bearing some similarities to the novaculite chert of McBride & Folk (1977). Bedding surfaces exhibit crowded randomly oriented lenticular pseudomorphs after gypsum and fine fractures (Fig. 6A). This suggests that lenticular gypsum crystal orientation and growth in sediments prior to silicification was also random. The surface fractures attain different shapes and sizes, and form veinlets filled mostly by length-fast chalcedony and megaquartz (Fig. 6B), but rarely contain length-slow chalcedony. Notably, these fractures are restricted to the porcelanite layers and do not extend into the carbonate layers of the couplets. This suggests that the porcelanite bed silicification pre-dated carbonate lithification, as observed by other authors (Chowns & Elkins, 1974; Geeslin & Chafetz, 1982).

The top and bottom few millimetres of beds in contact with the carbonate layers form an irregular white porous fringe with a sandy feel that contrasts with the smooth porcelanite bed texture. Under normal light, it is clear that the porcelanite bed boundary rim is undergoing recrystallization. It shows an abundance of silica spherules and microcrystalline quartz compared to the relatively darker opaline composition of the main porcelanite bed. The contact between the two textures is irregular with micro-protrusions and bays suggesting progressive replacement and recrystallization of the opaline porcelanite from the margin. The mostly isotropic opaline porcelanite groundmass also encloses scattered birefringent islands of various size and shape that attain similar texture to the fringe (Fig. 7A).

In plain light, the bed groundmass and the fringe are composed mainly of high relief spheroids surrounding lower relief microquartz crystallites in various proportions, and some sediment relics (Fig. 7B and C). The crystallites tend to coalesce into 20 to 50 μm anhedral, equant quartz with vague crystal boundaries and exhibit low birefringent length-slow brush extinction that has developed a characteristic speckled texture under crossed polars (Fig. 7D). In SEM images, these crystallites consist of packs of flaky parallel platelets that in places are reduced in size and number in favour of the spherules, due to the progressive conversion and replacement as observed in the fringe areas (Fig. 7E). The SEM–SEI–BSI microprobe spot analysis indicates that these spherules consist of 49.2 wt% Si and 50.8 wt% C, whereas, the associated quartz platelets consist of 55.5 wt% Si and 44.5 wt% C (Table 2). The crystallites are taken as metastable moganite crystals, such as those observed by Bustillo (2001). Optical microscopic examination of the porcelanite shows that there is an abundance of 2 to 3 μm dark, rounded possibly organic particles that occur as individuals or in clusters throughout the rock (Fig. 7B and C). These particles are

interpreted as fossilized bacteria such as those observed in ancient rocks (Perri & Tucker, 2007). In plain light, these particles attain high-relief and usually form the spherule's central cortex. In places, these particles are removed leaving the central cortex vacant. All of the spherule's outer shell jackets consist of radiating micro-fibrous length-slow chalcedony, enveloping the central cortex partly or completely (Fig. 7B and E). Elsewhere, high-resolution SEM photomicrographs show smaller particles about 25 nm in size, usually associated with fossilized EPS (extracellular polymeric substances), filamentous and coccoid bacteria (Figs 6F and 7F). Similar nano-spheres are described from modern microbial mats and interpreted as permineralized viruses that may act as nuclei for crystallite precipitation by Perri *et al.* (2018).

The porcelanite beds also enclose 0.1 to 0.5 mm, vertically oriented moulds that attain randomly shaped geometries with lobate sides (Fig. 7B). These cavities originated either as birds-eye trapped air bubbles or likely as pseudomorphs of minute gypsum crystals, which are commonly observed in the unaltered gypsiferous mudstone beds described earlier (Fig. 3A and B). Most of these cavities are lined by a 30 to 70 μm thick isopachous fringe of brown, fibrous quartzine that grew at a right angle to the cavity wall. In places, the quartzine is separated from the opaline wall by a 10 to 20 μm translucent weakly birefringent zone that extends around the cavity. These are analogues to those observed in the opaline nodule's lining of the shrinkage cracks (Fig. 3). The central cavities meanwhile, are filled by a single length-fast chalcedony with splaying fibrous extinction, or occasionally filled by microcrystalline quartz mosaic. The porcelanite beds are composed of up to 97% SiO_2 indicating that there are few or no other mineral components present (Table 1). The XRD analyses suggest an opal-CT composition, consisting of cristobalite, tridymite and quartz, in addition to traces of opal-A in some samples. Significantly, however, patterns obtained from the XRD analysis of some porcelanite samples that include associated pseudomorphs after gypsum show *d* spacing of peaks at around 4.448 Å, 3.108 Å and 2.883 Å, indicating moganite composition (Fig. 9). Meanwhile, other peaks indicate the presence of quartz and mixed quartz–moganite content. Further XRD refinement quantitative results confirmed the presence of 20.7 wt% moganite content in bedded porcelanite sample (Table 3). The fact that moganite is detected by modern XRD prior to the application of refinement techniques is attributed to the purity of the SiO_2 content in the porcelanite samples. Detection of moganite in some other Cyrenaican chert on the other hand, may be hampered by the dominant occurrence of other minerals in the samples.

Pseudomorphs after gypsum

The lenticular pseudomorphs after gypsum occur in silicified oolitic packstone (Fig. 4B) and in the porcelanite beds (Fig. 6A and B). They attain biconvex lens shapes that are up to 6 cm in diameter and 1.5 cm in cross-section at the centre. These are mostly oriented with their long axis perpendicular, at an angle, or lying parallel to the bedding plane (Fig. 6A). In the porcelanite – carbonate couplets, pseudomorphs retain their original lenticular crystal geometry with the enclosing porcelanite; however, their outline tends to fade in the carbonate beds (Fig. 6B). In the oolitic opaline nodules, pseudomorphs are completely occluded by randomly oriented lutecite bundles and ooids that were enclosed within the gypsum crystal during their displacive growth (Fig. 4B). The porcelanite pseudomorphs, on the other hand, demonstrate multi-stage diagenetic replacement and cavity-filling precipitation of silica minerals lining the margin, as their central cavities are partly to completely filled by mottled geopetal sediments cemented by translucent silica minerals (Fig. 8A).

Optical photomicrographs and SEM images of the fringe lining of the pseudomorphs consist of three basic successive textural layers of silica minerals (Fig. 8B). The early phases are exclusively related diagenetic replacement of gypsum, which correlates with those observed in the cavity-filling poikilotopic gypsum cement (Fig. 4). The first outer layer against the pseudomorph boundary is light tan, 0.08 to 0.4 mm thick lutecite representing the initial silica replacement phase of the gypsum crystal. The lutecite lining consists of two well-defined textural fabrics. The first on the outside consists of rosettes exhibiting curved radial-fibrous aggregates followed on the inside by straight parallel-blades of fibrous lutecite motif. These textural fabrics are separated by a narrow colourless translucent zone, which is either isotropic or exhibits vague wavy extinction independent of the orientation of lutecite fibres (Fig. 8B). This zone is observed in all thin sections examined. In places, where slivers from the enclosing sediments are detached during the growth of the gypsum crystal, it develops partly disconnected rosettes (Fig. 8C and D).

Blades of the lutecite fibrous motif pass into 0.1 to 0.2 mm thick moganite phase (Fig. 8B to D). It forms the transitional mineral phase in the replacement of poikilotopic gypsum by lutecite as described earlier (Fig. 4C and D). Moganite is an amorphous layer in normal light, but shows vague brush extinction in tandem with the lutecite under crossed polars as it wraps syntaxially on the lutecite (Fig. 8D). In contrast to the case of the cavity-filling poikilotopic gypsum cement (Fig. 4C), the pseudomorph moganite phase terminates by an irregular corrosion surface causing

thickness variations or complete removal. It marks the gypsum dissolution phase that also led to geopetal sediments collapsing into the vacant pseudomorph cavity (Fig. 8A). The gypsum dissolution is followed by precipitation of 70 μm thick, micro-layered minute quartz flakes alternating with isotropic opal (Fig. 8B to E). It is followed by a cavity filling phase of isopachous quartz palisade, that evolves into crudely stacked, fan-shaped, zoned quartz exhibiting length-slow brush extinction. This phase is similar to the undulose megaquartz of Milliken (1979), and identified as fortification quartz (McBride & Folk, 1977). The zonation bands of this phase are composed of 0.5 to 0.1 μm bubbles of fluid inclusions organized across the crystal c-axis (Fig. 8E). These pass gradually into clear palisades of prismatic megaquartz with euhedral pyramid face terminations pointing at the pseudomorph centre (Fig. 8F). The post-corrosion cavity filling mineral sequence exhibits textural variations in different pseudomorphs. Observed sequences may consist of length-fast chalcedony instead of zoned quartz, followed by quartzine and euhedral quartz; or in some cases it starts with chalcedony to zoned quartz and megaquartz.

DISCUSSION

Silicification paragenesis

The Cyrenaican chert suite has evolved during early silicification of sediments on the margins of the Messinian salinas. The varied SiO_2 mineralogical and textural phase development of the chert was controlled by the evolution of the prevailing diagenetic geochemical environmental conditions. This relationship is highlighted and summarized in a simplified flowchart (Fig. 10). The present study has established that the chert was developed in two stages; an early conversion and replacement stage, followed by dissolution and cavity-filling stage. In some cases, the second stage is absent, suggesting that the conversion stage is still ongoing. These two stages and their relative timing are illustrated graphically to demonstrate the mineralogical and textural paragenetic continuum of the Cyrenaican chert during silicification (Fig. 11). The SEM, optical microscopy and XRD analytical and refinement techniques confirmed the role of moganite as the main transitional silica phase in the conversion, replacement and recrystallization of mineral phases. This conclusion concurs with the results obtained from earlier studies (Heaney, 1995; Heaney & Post, 1992; Bustillo, 2001; Bustillo *et al.,* 2012).

Most authors recognize the role of opaline silica maturation in the formation of many quartz textures. However, with the exception of macrocrystalline and mesocrystalline quartz, most varieties of fibrous chalcedonic textures are found to contain moganite (Bustillo *et al.*, 2012), as indicated in the study of lutecite for example (Nagasi *et al.*, 2013). This led the authors to conclude that the initial recrystallization of opal into fibrous textures occurs through a transitional moganite phase. Field evidence suggests that silicification of the Cyrenaican opaline nodules is a near surface weathering phenomena. It pre-dates complete sediment lithification, as demonstrated in the deformation of ooids prior to opalization of oolitic deposits and silicification of gypsum (Fig. 4B). The replacement of gypsiferous mud, carbonates and organic matter by the waxy, amorphous opal-A, to develop opaline nodules is the earliest diagenetic silicification stage (Figs 3 and 11A). Silicification was initiated gradually on the outer surface of nodules during precipitation from supercritical silica-rich fluids in the sulphate-rich environment (Folk & Pittman, 1971; Laschet, 1984). The bedded porcelanite, on the other hand, represents a relatively advanced stage of opaline maturation. It consists primarily of opal-CT, which bears textural and mineralogical affinity to the opaline nodules (Fig. 11A and B). This is a continuum of the conversion and recrystallization of opal-A into opal-CT and other silica minerals during diagenesis (Greenwood, 1973). Water loss to evaporation during subaerial exposure is regarded as one of the main factors in the maturation and recrystallization of opal (Scurfield & Segnit, 1984). In all cases, evidence from the Cyrenaican opaline nodules and bedded porcelanite indicates that hardening due to silicification took place prior to lithification of the associated sediments (Knauth, 1979).

Dehydration shrinkage cracks in the opaline nodules and micro-cavities in the bedded porcelanite are lined by fibrous isopachous length-slow quartzine (Figs 3 and 7B). According to Folk & Pittman (1971), length-slow chalcedony precipitates from highly concentrated silica solutions by ionized tetrahedra units in a sulphate-rich environment and suggests that it occurred during evaporation. However, Chowns & Elkins (1974) and Laschet (1984) postulated that quartzine might form because of the conversion and recrystallization of opal. Observations from the Cyrenaica opaline chert support this notion, because evidence indicates that quartzine developed from the conversion of the opaline host through an intermediate moganite phase (Figs 3E, 3F and 7B). Recrystallization and conversion of a host rock into a new mineral phase is not an uncommon phenomenon during diagenesis of sedimentary rocks. In a study of dolomite evaporite solution collapse breccia, Moore (1971) reported that the diagenetic conversion of dolomite clasts margins

into pseudospar calcite occurs during dedolomitization. The pseudospar was previously interpreted as cavity filling cement. In the opaline nodule dehydration cracks, the isopachous quartzine is followed by silica gel (opal-AG) precipitation, which was later crystallizing to length-fast chalcedony (Fig. 11A). It also fills the porcelanite beds fractures and occludes micro-cavities (Fig. 7B). Opal-AG precipitates from highly concentrated silica solutions at low pH, and diluted sulphate content during flushing (Folk & Pittman, 1971; Laschet, 1984).

The pore network in the bioclastic carbonates allowed precipitation of poikilotopic gypsum crystals from groundwater supersaturated with respect to calcium sulphate in the phreatic zone. Petrographic, SEM and XRD analysis indicated that the original calcite shell fragments and matrix are dolomitized, and in various stages of replacement by gypsum and opaline silica. Whole shells and fragments were dolomitized during and/or soon after the precipitation of gypsum. Precipitation of gypsum led to relative depletion of Ca^{2+} and increase of Mg^{2+} ions in groundwater, and is regarded as the main cause of dolomitization in these rocks (Tucker, 1976b). By the introduction of silica-rich solutions, carbonate grains and matrix were replaced by amorphous opaline silica (Fig. 4B), which tends to recrystallize into microcrystalline quartz (Figs 4F and 11D). In contrast, lutecite forms by direct volume to volume replacement of the poikilotopic cement, and the lenticular gypsum crystals by silica to form pseudomorphs. In both cases, the progression of gypsum silicification proceeded through an intermediate moganite phase and accelerated along the weak pathways of the gypsum cleavage planes (Figs 4C, 11B and 11D). Taking into account that thin sections are cut across the nodule's outer rim at the interface with the gypsum (Fig. 4C and D); it shows not only the moganite transition, but also exhibits the lutecite textural change from rosette patterns to straight motif (Figs 8B, 8C, 11B and 11D). The textural change is attributed to the presence of inclusions within the gypsum at their boundary with the carbonates prior to silicification. It is also noted that the lutecite textural change occurs through an intermediate moganite phase (Figs 8 and 11B).

The preservation of the mineralogical sequence of poikilotopic gypsum to moganite and lutecite in the bioclastic carbonate rocks suggests that the diagenetic process is still active at near surfaces today. However, in the porcelanite – microbial carbonate couplets, seasonal fluctuations in groundwater levels, lowering of the salinity and subaerial exposure to meteoric water led to the complete dissolution of the gypsum before the conversion process by silica is concluded. The dissolution event is marked not only by the removal of gypsum, but also led to the corrosion of the

metastable moganite interface, leading to geopetal collapse of the insoluble content as well as silica debris in the pseudomorph cavity. The moganite corrosion boundary separates the diagenetic replacement phase from the cavity-filling phase within the pseudomorphs (Fig. 11B). This boundary also correlates to the boundary between the diagenetic replacement of the quartzine phase, and the cavity-filling phase of length-fast chalcedony observed in the opaline nodules cracks during freshwater flushing (Fig. 11A). Pseudomorphs observed in the oolitic opaline nodules, on the other hand, are completely filled by interlocking lathes of lutecite crystals (Fig. 4B); indicating that silicification of gypsum was concluded prior to salinity flushing. In all cases, moganite played a crucial role as a transitional agent in the conversion of opal into quartzine (Fig. 11A), replacement of gypsum by lutecite (Fig. 11C and D), and it forms the transition between different lutecite fabrics (Figs 8C and 11B).

Based on the Cyrenaican chert Al/Si ratio analysis data, Amrouni *et al.* (2015; 2016b) concluded that silica was derived primarily from a continental source. It is conceivable that the majority of samples used in this study were collected from carbonate units south of the study area where siliciclastic deltaic deposits are common. However, this conclusion does not negate the possibility of an organic origin of the silica in the bedded porcelanite that is commonly found above the thick selenite bodies in the distal north of the study area (Figs 1C and 2). Diatoms could have been a silica source for the bedded porcelanite and nodules associated with microbial laminites and stromatolites in this part of the study area (Fig. 1A). Modern hypersaline salinas are commonly fed from freshwater karstic springs, allowing diatoms to thrive in association with subaqueous mats and microbial cyanobacteria at their margins in Western Australia (Savage & Knott, 1998).

The role of organic matter in silicification

Organic matter such as EPS, bacteria and viruses played an essential role in sedimentation and diagenesis in the lagoonal facies complex of Wadi al Qattarah Formation in Cyrenaica. These elements are observed in outcrops as microbial laminites and stromatolites, and on a microscopic scale as microbial filaments and particles in crystalline gypsum, carbonates and chert. The experimental work of Birnbaum & Weirman (1985), suggested that the degradation of organic matter by sulphate reducing bacteria plays a significant role in the silicification of evaporites. A

study by Perri *et al.* (2018) confirmed the role played by microbial filaments, bacteria, viruses and EPS in carbonate and silica biomineralization in modern sabkha microbial mats. Alonso-Zarza *et al.* (2002) attributed dolomitization and silicification of terrestrial anhydrite nodules to the presence of sulphate reducing organic elements and bacteria. Also, rich microbial populations are found embedded within the Messinian selenite of Italy, where some of the filamentous bacteria attain mineralized outer sheaths of calcite, dolomite or pyrite (Panieri *et al.,* 2008). A recent study of bedded chert–dolomite cycles in the Eocene Green River Formation (USA) attributes the precipitation of lacustrine chert to the decomposition of microbial organic matter (Kuma *et al.*, 2019). In addition, the presence of organic matter around the foliated crystallite microstructure of shells is found to be the preferred nucleation site of silicification (Elorza & Orue-Etxebarria, 1985; Mišík, 1995; Daley & Boyed, 1996; Butts, 2014).

The present study demonstrated that organic matter enveloping gypsum pseudomorphed foliated oyster shell microstructure is preferentially replaced by moganite that was later converted into lutecite (Figs 5 and 11C). In the bedded porcelanite, fossilized bacteria acted as centres of crystallization for radiating micro-fibrous length-slow chalcedony forming spherules surrounded by and replacing moganite (Fig. 7). Silicified streaks and layers in the coarsely crystalline carbonate beds consist mostly of silicified EPS sheets, (possibly) filamentous fungi; filamentous and coccoid bacteria that also include nanoparticles interpreted as viruses (Figs 6E, 6F, 7C and 7F).

Climatic control of sedimentation and silicification

The Cyrenaica lagoonal facies deposition and diagenesis took place in conditions similar to the present-day coastal lagoons and sabkhas of the Gulf of Sirt of Libya (Sherif, 1978) and the salina lakes of southern Australia (Von der Borch *et al.*, 1977; Gostin *et al.*, 1988). The Cyrenaican giant selenite crystal palisades are interrupted by laminae forming successive Fe-stained dissolution surfaces, clotted microbial inclusions, and are followed by clear syntaxial gypsum crystal overgrowths of various thicknesses (Fig. 2C). The crystal dissolution–microbial–crystallization mini-cycles depict the fluctuating wet and evaporitic cyclic conditions in response to climatic episodes affecting most lagoonal salinas (Hardie & Eugster, 1971; El-Hawat, 1980; Rouchy & Monty, 2000). In the field, it is possible to measure the thickness of these mini-cycles and semi-quantitatively group them into thin (average 7.0 mm) and thick (average 33.5 mm) cycles.

Variations in the thicknesses of these cycles are taken to reflect the fluctuation of intensity and duration of each phase in response to the prevailing seasonal climatic conditions during the Messinian. In addition, obtained unpublished sulphur isotope analysis data of the Cyrenaican selenite samples provided average $\delta^{34}S$ values of 23.3‰, indicating that gypsum subaqueous crystallization took place from brackish water as a result of a mixing of marine and fresh waters. Similarly, sulphur isotope analysis of coarsely crystalline gypsum from the Quaternary sabkhas on the coast of the Gulf of Sirt of Libya gave $\delta^{34}S$ values of 20.3‰ (Rouse 1977; Sherif, 1978). These sabkhas are flooded seasonally by mixed marine–continental groundwater that percolates upward through sediments from karstified Tertiary substrates and from local springs (Sherif, 1978).

The alternation of bedded porcelanite – microbial carbonate couplets with stromatolite beds also represents depositional phases of climatically controlled seasonal flooding and evaporation cycles. Whereas stromatolites were developed in the submerged areas during wet seasons, the microbial mats and mud are favoured during drier climatic conditions at the salina margins. The diagenetic history revealed from the associated pseudomorphs after gypsum also indicates variations in salinities in the marginal flats. Such conditions of fluctuating salinities and seasonal groundwater level oscillations influence evaporite precipitation, diagenesis and freshwater dissolution (Warren, 2006). These are records of the dry arid to wet semi-arid climatic fluctuations, which dominated Europe (Böhme *et al.,* 2011) and North Africa (Hounslow, *et al.*, 2017) during the Miocene, and particularly during the onset of the Messinian salinity crisis in the Mediterranean (Manzi *et al.,* 2013).

CONCLUSION

The Cyrenaican chert represents a continuum of early silicification of marginal lagoonal deposits since the Messinian that is still active at near-surface conditions to the present day. The optical and X-ray diffraction (XRD) techniques documented that moganite acted as the main transitional agent in the replacement and conversion of one mineral phase to another. This study contributes to further current understanding of the relationship of length-slow chalcedony (quartzine and lutecite) and evaporites, as previewed in the *Introduction*. The length-slow fibrous quartzine develops during the diagenetic replacement of opaline material through a moganite phase. It is followed by cavity-filling precipitation of translucent silica gel that converts into length-fast

chalcedony. Lutecite, on the other hand, is the product of early diagenetic silicification of poikilotopic gypsum, that infilled pore spaces and pseudomorphed shells, through moganite transition. Organic matter, microbial filaments and coccoid bacteria acted as centres of moganite nucleation and played an essentially active role in the silicification process. Pseudomorphs after large lenticular gypsum crystals host the record of the textural and mineralogical continuum reflecting stages of gypsum replacement by moganite and lutecite, through to gypsum dissolution, and precipitation of a variety of cavity-filling euhedral quartz palisades in response to lowering of salinity and fluid flushing.

ACKNOWLEDGEMENTS

Research on the Miocene in Cyrenaica was supported by the University of Benghazi (Garyounis) Research Centre, Libya. ASH is indebted to Prof. Dr F.M. Thiedig, formerly of the University of Hamburg, Germany, for providing thin section, SEM facilities, and gypsum isotope analysis data that initiated this study. Dr H. Nielsen conducted sulphur isotope analysis on gypsum samples. XRD and XRF analysis were conducted by Mr S. Al-Mamari, and additional thin-section preparations are made by Mr H. Al-Zaidi, both are at Sultan Qaboos University research laboratory facilities, Oman. Dr S. McLaren wishes to thank Prof. S. Davies for helping to support funding of XRD analysis at the BGS (UKRI). Dr S.J. Kemp carried out quantitative and qualitative XRD analyses and publishes with the permission of the Director, British Geological Survey (UKRI). We would like to extend our thinks to Dr F. Scheffler and an anonymous reviewer for their objective comments that contributed to the improvement of the manuscript. We also appreciate the help and support of Prof. M.J. Salem of University of Tripoli, Libya.

REFERENCES

Alonso-Zarza, M. Nchez-Moya, S.A. Bustillo, M.A. Sopena, A. and Delgado, A. (2002) Silicification and dolomitization of anhydrite nodules in argillaceous terrestrial deposits: an example of meteoric-dominated diagenesis from the Triassic of central Spain. *Sedimentology,* 49, 303–317.

Amrouni, K.S. (2015) Sedimentology, sequence stratigraphy, and diagenesis of the Cyrenaican Miocene, Al Jabal Al-Akhdar uplift and Soluq Trough. Ph.D. unpublished dissertation, *Texas A&M University*. 172 pp.

Amrouni, K.S. Pope, M.C. El-Hawat, A.S. Obeidi, A.A. Amer, A. El-Bargathi, H.S. El-Jahmi, A.M. Al-Alwani, A.A. Elbileikia, E.A. and Mustafa, K.M. (2016a) Paleoshoreline and prograding clinoforms of oolitic grainstones of the Miocene carbonate-evaporitic sequences of the Ar-Rajmah Group, Al-Jabal Al-Khdar Uplift and Soluq Trough, Cyrenaica, NE Libya: *Gulf Coast Association of Geological Societies Transactions*, 66, 15–28.

Amrouni, K.S. Pope, M.C. El-Hawat, A.S. Amer, A. Elbileikia, E.A. El-Bargathi, H.S. Obeidi, A. A. Shaltami, O.R. Mustafa, K. M. Al-Alwani, A.M.A. El-Jahmi, A.M. El-Ekhfifi, S.A. and Wehner, M.P. (2016b) Silicification in the Cyrenaican Miocene carbonate-evaporite sequence, NE Libya: Origin, occurrence, facies, and sea level relationship. *Gulf Coast Association of Geological Societies Transactions*, 66, 29–38.

Bandel, K. Dullo, W-C. and Gaziry, A.W. (1986) unusual transformation of $CaCO_3$ and $CaSO_4$ with preservation of original structure. *Mitt. Geol. Paläont. Inst. Univ. Hamburg.* 61, 21-33.

Birnbaum, S.J. and Wireman, J.W. (1985) Sulfate-reducing bacteria and silica solubility: a possible mechanism for evaporite diagenesis and silica precipitation in banded iron formations. *Can. J. Earth Sci*., 22,1904-1909.

Böhme, M. Winklhofer, M. and Ilg, A. (2011). Miocene precipitation in Europe: Temporal trends and spatial gradients. *Palaeogeo. Palaeoclim., Palaeoeco*. 304, 212–218

Bustillo, M.A. (2001) Cherts with moganite in continental Mg-clay deposits: an example of ‘‘false’’ Magadi-type cherts, Madrid Basin, Spain. *J. Sed. Res.*, 71, 3, 436–443.

Bustillo, M.A. (2002) Appearance and significance of the moganite in the silica rocks: a review. *Journal of Iberian Geology*, 28l.

Bustillo, M. A. Pérez-Jiménez, J. L. Alonso-Zarza, A. M. and Furio, M. (2012) Moganite in the chalcedony varieties of continental cherts (Miocene, Madrid basin, Spain). Spectroscopy Letters, 45, 2, 109-113.

Butts, S.H. (2014) Silicification. In: Reading and writing of fossil record: Preservational pathways to exceptional fossilization (Eds M. Laflamme, J.D. Schiffbauer, and S.A.F. Darroch), *The Paleontological Society Papers*. 20, 15-33.

Cesarano, M. Bish D.L. Cappelletti P. Cavalcante F. Belviso C. and Fiore S. (2018) Quantitative of clay-rich siliciclastic landslide terrain of the Sorrento Peninsula, Italy using a combined XRPD and XRF approach. *Clays and Clay Minerals,* 66, 4, 353-369.

Chafetz, H.S. and Zhang, J.L. (1998) Authigenic megaquartz crystals in the Quaternary dolomite. *J. Sed. Res*. 68, 994-1000.

Chowns, T.M. and Elkins, J.E. (1974) The origin of quartz geodes and cauliflower cherts through the silicification of anhydrite nodules. *J. Sed. Petrol.*, 44, 885–903.

Daley, R.L. and Boyd, D.W. (1996) The role of skeletal microstructure during selective silicification of brachiopods. *J. Sed. Res.,* 66/1, 155-162.

El-Hawat, A.S. (1980) Intertidal and storm sedimentation of Wadi al Qattarah Member, Ar-Rajmah Formation, Miocene, Al Jabal al Akhdar. In: *Geology of Libya*, (M. J. Salem & M.T. Busrewil Editors). Academic Press, London. II, 449-462.

El-Hawat, A.S. and Salem, M.J. (1987) A Case Study of the stratigraphic subdivision of Ar-Rajmah Fm. and its Implication on the Miocene of Northern Libya. *Proc. VIIIth Cong. Med. Neogene Stratig*., Ann. Inst. Geol. Publ. Budapest, Hungary. LXX: 173-184.

El-Hawat, A.S. Barghathi, H. and Obeidi, A. (2004) Cyrenaica - Transect VII. In: *The Transmed Atlas: the Mediterranean Region from Crust to Mantel.* (Eds W. Cavazza, F. Roure, W. Spakman, G. Stampfli, and P. Ziegler), CD Rom. Springer-Verlag. 156pp.

El Khoriby E.M. (2005) Origin of the gypsum-rich silica nodules, Moghra Formation, Northwest Qattara depression, Western Desert, Egypt. *Sedimentary Geology*, 177, 41 – 55.

El Qot, G.M. Abdulsamad, E.O. and El Fakhry, A. (2017) Shell concentrations from the Miocene Ar Rajmah Group at Soluq-Al Abyar road cut, southern Al Jabal Al Akhdar, NE Libya. *Arab. J. Geosci*. 10:47, 1-15.

Elorza, J. and Orue-Etxebarria, X. (1985) An example of silicification in Gryphea sp. shells from Lano (South of Victoria, Spain). *6th Eur. reg. meeting of sed. I.A.S*., *Lleida* (Spain), 556-559.

Folk, R.L. and Pittman, J.S. (1971) Length-slow chalcedony: a new testament for vanished evaporites. *J. Sed. Petrol*., 41, 1045–1058.

Folk, R.L. and Weaver, C.E. (1952) A Study of the Texture and Composition of Chert. *Am. Jour. Sci*., 250:498-510.

Geeslin, J.H. and Chafetz, H.S. (1982) Ordovician Aleman Ribbon Cherts: an example of silicification prior to carbonate lithification. *J. Sed. Petrol*., 52, 1283–1293.

Gostin, V.A. Belperio, A.P. and Cann, J.H. (1988) The Holocene non-tropical coastal and shelf carbonate province of Southern Australia. *Sed. Geol.*, 60, 51-70.

Greenwood, R. (1973) Cristobalite: its relationship to chert formation
In selected samples from the deep sea Drilling project. *J. Sed. Petrol*., 43/3, 700-708.

Hardie, L.A. and Eugster, H.P. (1971) The depositional environment of marine evaporites: a case for shallow clastic accumulation. *Sedimentology*, 16, 187-220.

Hasse, R. (1989) Silica diagenesis: origin of inorganic and replacement chert. Earth-Sci. Rev., 26, 253-284.

Heaney, P.J. (1995) Moganite as an indicator for vanished evaporites: a testament reborn? *J. Sed. Petrol*., 65, 633-638.

Heaney, P.J. and Post, J.E. (1992) The widespread distribution of novel silica polymorph in microcrystalline quartz varieties: *Science*, 225, 441-443.

Hounslow, M.W. White, H.E. Drake, N.A. Salem, M.J. El-Hawat, A. McLaren, S.J. Karloukovski, V. Noble, S.R. and Hlal, O. (2017) Miocene humid intervals and establishment of drainage networks by 23 Ma in the central Sahara, southern Libya. *Gondwana Research*, 45 / 118–137.

Jacka, A.D. (1974) Replacement of fossils by length-slow chalcedony and associated dolomitization: *J. Sed. Petrol.*, 44, 421-427.

Keene, J.B. (1983) Chalcedonic quartz and occurrence of quartzine (length-slow chalcedony) in pelagic sediments: *Sedimentology*, 30:449-454.

Kemp, S.J. Wagner, D. Mounteney, I., Bell, C.P. Milne, C.J., Gowing, C.J.B. and Pottas, T.L. (2016) An improved approach to characterise potash-bearing evaporite deposits, evidenced in North Yorkshire, UK. *Economic Geology*, 111(3), 719–742.

Knauth, L.P. (1979) A model for the origin of chert in limestone: *Geology*, 7, 274-277.

Kuma, R. Hitoshi, H. Yamamoto, K. Yoshida, H. Whiteside, J.H. Katsuta, N. Ikeda, M. (2019) Biogenically induced bedded chert formation in the alkaline palaeo-lake of the Green River Formation. *Scientific Reports*. 9:16448.

Laschet, C. (1984) On the origin of Cherts. *Facies*, 10, 257-290.

Manzi, V. Gennari, R. Hilgen, F. Krijgsman, W. Lugli, S. Roveri, M. and Sierro, F. J. (2013) Age refinement of the Messinian salinity crisis onset in the Mediterranean. *Terra Nova*, 0, 1-8.

McBride, E.F. and Folk, R.L. (1977) The Caballos Novaculite revisited: Part II: chert and shale members and synthesis: *J. Sed. Petrol.*, 47, 1261-1286.

Miehe, G. and Graetsch, H.A. (1992) Crystal structure of moganite: A new structure type for silica. *Eur. J. of Mineral.*, 4, 692-706.

Milliken, K.L. (1979) The silicified evaporite syndrome – two aspects of silicification history of former evaporite nodules from southern Kentucky and northern Tennessee. *J. Sed. Petrol.*, 49, 245–256.

Mišík, M. (1995) Selective silicification of calcitic fossils and bioclasts in the west-Carpathian limestones. *Geol. Carpath.*, 46/3, 151-159.

Moore Jr., C.H., (1971) Pseudospar dedolomite "cements" of evaporite solution collapse breccias; in Carbonate Cements (Ed.O.P. Bricker), *John Hopkins Univ. Studies in Geology,* 19, 345-331.

Nagasi, T. Momma, K. Kuribayashi, T. and Tanak, M. (2013) Texture of lutecite. *J. Mineral. Petrol. Sci.,* 108, 87-93.

Panieri, G. Lugli, S. Manzi, V., Palinska, K.A. Roveri, M. (2008) Microbial communities in Messinian evaporite deposits of the Vena del Gesso (northern Apennines, Italy). *Stratigraphy, 5/3-4, 343-352.*

Perri, E. Tucker, M. (2007) Bacterial fossils and microbial dolomite in Triassic stromatolites. *Geology*, 35/3; 207–210

Perri, E. Tucker, M.E. Słowakiewicz, M. Whitaker, F. Bowen, L. and Perrotta, I.D. (2018) Carbonate and silicate biomineralization in a hypersaline microbial mat (Mesaieed sabkha, Qatar): Roles of bacteria, extracellular polymeric substances and viruses. *Sedimentology*, 65, 1213–1245.

Roemers-Oliveira, E. Fernandes, L.A. Freire, E.B. Simões, L.S.A. (2015) Microbial filaments in stromatolites and laminites of Balbuena III Sequence (Maastrichtian/Danian) of Yacoraite Formation in Metán-Alemania Sub-basin, Salta region, Argentina, and its palaeoenvironmental significance. *Brazilian Journal of Geology*, 45,3, 399-413.

Rouchy, J.M. Monty, C. (2000) Gypsum microbial sediments: Neogene and modern examples. In *Microbial sediments* (Ed. R.E. Riding and S.M. Awramik.). 211-216.

Rouse, J.E. (1977) A preliminary report of the sources of sulphate supply to the sabkhas of the western Gulf of Sirte, Libya. *Instit. Geol. Science. Isotope Geology Unit.* Stable Isotope Report No.18, 17p. (Unpublished).

Savage, A. and Knott, B. (1998) *Artemia Parthenogenetica* in Lake Hyward, Western Australia. II Feeding biology in seasonally stratified hypersaline lake: *Inter. J. Salt Lake Res.* 7, 13-24.

Scheffler, F. Immenhauser, A. Pourteau, A. Natalicchio, M. Candan, O. Oberhänsli, R. (2019) A lost Tethyan evaporitic basin: Evidence from a Cretaceous hemipelagic meta-selenite–red chert association in the Eastern Mediterranean realm. Sedimentology, 66/7, 2627-2660.

Shaltami, O.R. Fares, EL Oshebi F.F., Errishi, F.M., Bustany, H., Salloum, F.S., El Shawaihdi, M.H. and Musa, M.M. (2018) Absolute age of the Miocene deposits in the Cyrenaica basin, NE Libya: implications for the Messinian Salinity Crisis (abstract). *Irish Asso. Econ. Geol. (IAEG) annual conference - geochemistry*.

Sherif, N. (1978) Quaternary sedimentation of the western coast of the Gulf of Sirte, Libya. *University of London*, Unpublished PhD Thesis, 263 pp.

Schmitt, J.G., and Boyd, D.W (1981) Patterns of silicification in Permian pelecypods and brachiopods from Wyoming: *J. Sed. Petrol.*, 51, 1297-1308.

Scurfield, G. and Signit, E.R. (1984) Petrification of wood by silica minerals. *Sed. Geol*. 39-3/4, 149-167.

Siedlecka, A. (1972) Length-slow chalcedony and relicts of sulfates – evidence of evaporitic environments in the Upper Carboniferous and Permian red beds of Bear Island, Svalbard. *J. Sed. Petrol*., 42, 812–816.

Siedlecka, A. (1976) Silicified Precambrian evaporite nodules from northern Norway: a preliminary report. *Sed. Geol*., 16, 161–175.

Snyder, R.L. and Bish, D.L. 1989. Quantitative analysis. In: D.L. Bish, and J.E. Post, (Eds.), *Modern Powder Diffraction, Reviews in Mineralogy*, Volume 20, Chapter 5, Mineralogical Society of America, USA, pp. 101–144.

Tucker, M.E. (1976a) Quartz replaced anhydrite nodules ('Bristol Diamonds') from the Triassic of the Bristol District. *Geol. Mag*., 113, 569–574.

Tucker, M.E. (1976b) Replaced evaporites from the late Precambrian of Finnmark, Arctic Norway. *Sed. Geol*., 16, 193–204.

Ulmer-Scholle, D., Scholle, P.A. and Brady, P.V. (1993) Silicification of evaporites in Permian (Guadalupian) back-reef carbonates of the Delaware Basin, West Texas and New Mexico. *J. Sed. Petrol*., 63, 955–965.

Von der Borch, C.C. Bolton, B. and Warren, J.K. (1977) Environmental setting and microstructure of subfossil lithified stromatolites associated with evaporites, Marion Lake, South Australia. *Sedimentology*, 24, 693-708.

Warren, J.K. (1991) Sulfate dominated sea-marginal and platform evaporative settings. In: Evaporites, Petroleum, and Mineral resources (J.L. Melvin, ed.): *Developments in Sedimentology,* Amsterdam, Elsevier, 50, 477-533.

Warren, J.K. (2006) Evaporites; Sediments, Resources and Hydrocarbons. *Springer*, 1035pp.

Warren, J.K. (1982) The hydrological significance of Holocene tepees, stromatolites, and boxwork limestones in coastal salinas in South Australia: *J. Sed. Petrol.*, 52, 1171–1201.

West, I. (1964) Evaporite diagenesis in the Lower Purbeck beds of Dorset. *Yorks. Geol. Soc. Proc.* 34/15:315–332.

West, I. (1973) Vanished evaporites-significance of strontium minerals. *J. Sed. Petrol.*, 43/1: 278-279.

FIGURE CAPTIONS

Figure 1. Location map **(A),** showing the Miocene geology of Cyrenaica, north-east Libya, and the location of measured sections. Sections with asterisks are locations of studied chert samples. **(B)** Generalized stratigraphic cross-section of Ar-Rajmah Group formations (modified from El-Hawat & Salem, 1997). The inserted column in section 6/7 is detailed in (C). **(C)** Measured section in Hawa al-Barraq gypsum quarry illustrating the lagoonal salina selenite and marginal carbonate facies succession.

Figure 2. **(A)** Hawa al-Barraq quarry view of giant selenite deposits overlain by marginal carbonates as depicted in the log (Fig. 1C). The quarry was opened in a collapsed doline. The crystalline gypsum sequence is interrupted by a storm reworked gypsarenite layer (yellow arrow heads). Vertically oriented crystals glisten by light reflection on the prominent (010) gypsum cleavage surface (white arrows). Jacob's staff scale is 1.5 m. **(B)** Selenite crystals are cyclically interrupted by microbial laminae inclusions enhanced by differential weathering. **(C)** Photomicrograph of a mini-cycle in selenite crystal (1) illustrating a micro-sequence of dissolution surface (arrows), followed by an initial syntaxial crystal growth (2), microbial layer disrupted by crystal growth (3), followed by continued crystal growth (4); all are in optical continuity. **(D)** Outcrop of the marginal carbonate beds above the gypsum. Arrows point to bedded porcelaneous chert interbedded with stromatolite (St) and overlain by a stromatolite exhibiting complex brecciation and silicification patterns. Scale is 10 cm divisions. **(E)** Outcrop of soft gypsiferous mudstone (1), deformed evaporite-solution collapsed carbonates and tepee-structure (2), the dotted line and arrows point at chert nodules in gypsiferous coarse bioclastic lag bed. The section is capped by coarsely crystalline gypsum bed (3). Scale at the centre is 80 cm.

Figure 3. **(A)** Photomicrograph of gypsiferous mudstone showing a nodule of minute gypsum crystals, microbial grains and oncoids (arrow). Natural light (NL). (B) Silicified minute lenticular gypsum clusters (arrows) encased in mud matrix (dark areas) of opaline nodule. **(C)** Scanning electron microscope (SEM) micrograph of silicified microbial oncoid, arrows point to spot microprobe analysis cites (see Table 2). **(D)** SEM micrograph of opaline chert nodule (2) showing botryoidal structure of fibrous quartzine radiating from the shrinkage crack cavity wall (1). **(E)** Close-up of an opaline chert nodule's wall (1), lined by quartzine crystal fringe (2). The quartzine encloses a detached inclusion from the wall (white arrow) and is followed by amorphous translucent silica-gel showing a serrated surface (black arrow) growing into the central cavity (3),

NL. **(F)** Close-up of opaline nodule's shrinkage crack (1), lined by quartzine (2) and underlain by a transparent moganite zone (arrows). The centre of the cavity is filled by SiO_2 gel with trapped bubbles of fluid inclusions (3), NL. **(G)** Photomicrograph of a shrinkage crack in an opaline nodule (1), lined by isopachous quartzine fringe (black arrow), and separated from the opaline host by a discontinuous birefringent moganite zone (white arrow). Length-fast chalcedony splays (2) and cavity fill of geopetal sediment at centre (3). Crossed nicols. **(H)** High resolution SEM of cone-shaped fibrous length-fast chalcedony bundle. Individual fibres consist of stacked quartz crystallites with their elongation normal to the fibrous growth direction (arrows).

Figure 4. **(A)** Coarse bioclastic limestone cemented by large poikilitic gypsum crystals showing patchy light reflection on (010) cleavage surfaces (1), white arrows and dotted line mark the boundary between crystals of different orientation (2). The dark chert nodule (3) is in the process of replacing the carbonate grains and gypsum cement. The black arrow points at the nodule's white rim. **(B)** Deformed opaline oolitic packstone encloses pseudomorphed lenticular gypsum filled by lutecite (arrow), natural light. **(C)** Photomicrograph of the chert nodule's outer rim illustrating the boundary with poikilotopic gypsum cement. It is showing fibrous lutecite (1), with zigzagged terminations (2). These pass into a clear moganite zone (3) exhibiting a pseudo-crystal termination controlled by the gypsum cleavage planes (4), and carbonate grain inclusions (5). **(D)** Image (C), crossed nicols. **(E)** Scanning electron micrograph of a freshly fractured nodule surface showing well-defined lutecite fibre bundles (3), passing into low relief moganite zone (2). The well-defined moganite-gypsum boundary is and controlled by gypsum cleavage (1). **(F)** Photomicrograph of the nodule's core displaying an advanced silicification stage, observed with crossed nicols and first-order red retardation plate inserted from the south-east corner. Carbonate grains are replaced by microcrystalline quartz (1), intergranular porespaces are lined by multi-generation lutecite fringe (2), the central porespace is filled by moganite (3), that encloses poikilotopic gypsum cement relics (arrows).

Figure 5. **(A)** High resolution scanning electron microscopy (SEM) micrograph of the gypsum–silica interface showing gypsum (1) and lutecite or moganite? (2), demonstrating a characteristic flaky and porous 'Weetabix' SiO_2 texture. **(B)** High resolution SEM micrograph showing the relation between gypsum (1) and moganite (2) as both are penetrated by microbial boring tunnels filled by fossilized cyanobacteria particles (arrows). **(C)** Photomicrograph of gypsum pseudomorphed shell (4) retaining the outer microbially micritized envelope (3) and lozenges of

lutecite beekite texture (1). Moganite (2) forms a transitional zone between the two minerals. The moganite–lutecite boundary is sharp (arrow), NL. **(D)** Image (C), crossed nichols (XN). **(E)** Close-up of the shell microbial envelope (3) showing extensive microbial boring tunnels (arrows). The host shell is replaced by lutecite (1), and moganite (2) forms distinctive patchy smooth texture that does not retain any of the poikilotopic gypsum texture (4). **(F)** Image (E), XN.

Figure 6. (A) Plane view of porcelanite chert bed showing exhumed pseudomorphs after lenticular gypsum crystals, the dark khaki green clay covered area between the pseudomorphs. Pseudomorphed crystals are oriented vertical (black arrows) or horizontal (white arrows) in relation to the bedding plane. **(B)** Lateral view of a porcelanite–carbonate couplet with pseudomorphs after lenticular gypsum (arrows). **(C)** Scanning electron microscopy (SEM) micrograph of zoned blocky calcite spar (1), and flaky silica masses (2). The calcite crystals display extensive corrosion notches where silica replaces calcite (arrows). **(D)** SEM image showing calcite crystal (1) encased and is in the process of being replaced by silica (2) through micro-fibrous front (arrow). **(E)** SEM photomicrograph of silicified streak in carbonate layer, exhibiting thick filamentous fungal? structure (black arrow points to spot analysis C 27.7 wt%, Si 25.5 wt%), clusters of 25 nm viral spheroids (white arrows), overlain by a degraded silicified organic matter (dashed arrow). A detail of the framed insert is shown in (F). **(F)** Close-up of the viral aggregates (white arrow), showing the degraded ESP (extracellular polymeric substance), that consists of amalgamated granular nanno-particles and filaments (dashed arrow). The black arrow left of the image points to a partial view of a filament with hollow centre.

Figure 7. **(A)** Photomicrograph of the lower section of porcelanite bed consisting of dark opaline silica (2) overlaying lighter recrystallized base (1). The replacement boundary between the two textures is irregular (black arrow). The gypsum pseudomorph boundary is sharp (white arrow) and showing marginal crystalline filling fringe (3) and central cavity (4). Bed top is to the right, crossed nichols (XN). **(B)** Photomicrograph in the porcelanite bed groundmass showing micro-cavity lined by isopachous quartzine (black arrow) and filled by transparent length-fast chalcedony (1). The porcelanite texture consists of spheroidal fabric surrounded by translucent anhedral microcrystalline quartz, possibly moganite. The spheroidal cortex is occupied by coccoid bacteria surrounded by outer shell of radial length-slow fibrous fringe of quartzine or lutecite (white arrow), natural light (NL). **(C)** Photomicrograph of microbial bacterial clusters (black arrows) surrounded by micro-fibrous quartzine and low relief anhedral microcrystalline moganite (white

arrows), and some relics of original sediments (s), NL. **(D)** Image (C), showing speckled texture with birefringent moganite exhibiting wavy extiction, XN. **(E)** Scanning electron microscopy (SEM) photomicrograph and spot microprobe analysis of the spheroids (C 50.8 wt%, Si 49.2 wt%), are surrounded by smooth platy texture of moganite (Si 55.5 wt%, C 44.5 wt%). **(F)** High resolution SEM image showing microbial clusters associated filaments (arrows).

Figure 8. (A) A close-up view of a pseudomorph after gypsum in a porcelanite bed (arrow) showing a dark fringe of the early phase of gypsum replacement by silica followed by white inner zone of quartz, and followed by silicified geopetal cavity filling (arrow). **(B)** Enlarged photomicrograph of the dark fringe showing silica textural variations of the early phase of gypsum replacement by lutecite, illustrating a sequence of opaline porcelanite bed forming a smooth boundary with the pseudomorph (1), lutecite (rosettes 2 and bladed texture 3), moganite (4), corrosion zone (black arrow) and zoned quartz (5). Note the change between lutecite textures is marked by isotropic boundary (white arrow), crossed nichols (XN). **(C)** Photomicrograph illustrating the textural sequence formed around a detached and recrystallized sliver from the pseudomorph wall (1), followed by a lutecite phase (2) interrupted by a thin translucent moganite layer (black arrow) and moganite zone (3). The corrosion zone (white arrow) is followed by palisade of isopachous quartz and zoned mega-quartz (4), and central cavity (5), natural light. **(D)** Image (C), XN. **(E)** Scanning electron microscopy (SEM) close-up of the corrosion micro-layered zone showing alternating opal and microcrystalline quartz (1), the zoned megaquartz is lined by fluid inclusions (2). **(F)** SEM image of the layers above the corrosion zone showing rows of microcrystalline quartz (1), opaline zone (2), zoned mega quartz (3) and cavity filling euhedral megaquartz (4).

Figure 9. Powder X-ray diffraction patterns of the bedded porcelanite and associated pseudomorphs after gypsum showing moganite at peaks 4.448 Å, 3.108 Å and 2.883 Å. Other peaks points to quartz and quartz–moganite association (MQz).

Figure 10. Simplified flowchart explains the SiO_2 mineral phase evolution of the Cyrenaican chert varieties under changing geochemical environmental conditions.

Figure 11. Schematic illustration of Fig. 10 demonstrating the mineralogical and textural fabric phase development detailed in Figs 3, 4, 5 and 8 where moganite forms the transition phase in mineral replacement and conversion. **(A)** The opaline nodule's crack wall. **(B)** Lenticular gypsum

pseudomorph inner margin. **(C)** Silicification of gypsum pseudomorphed oyster shell. **(D)** Silicification of cavity filled poikilotopic gypsum cement.

TABLE CAPTIONS

Table 1. X-ray fluorescence (XRF) chemical composition analysis (in weight %) of chert nodules and associated carbonate samples.

Table 2. Scanning electron microscopy – secondary electron imaging – backscatter image analysis (SEM–SEI–BSI) semiquantitative analysis results for oxygen, carbon, silicon, calcium, aluminium, magnesium and iron (in weight %) from chert nodules and stromatolite samples.

Table 3. Summary of qualitative and quantitative X-ray diffraction (XRD) analyses (in weight %).

Table 3. Summary of qualitative and quantitative X-ray diffraction (XRD) analyses (in weight %).

TABLES

Table 1

Samples	Opal nodules	Chert in poikilotopic gypsum		Porcelaneous chert with pseudomorphs				Microbial carbonate beds	
Elements	**ES-1**	**S5-20a**	**S5-20b**	**HB-1b**	**HB-2a**	**HB-2b**	**HB-3**	**HB-1a**	**HB-1c**
SiO_2	82.83	44.10	57.16	90.44	96.88	96.10	77.39	8.06	6.22
TiO_2	0.01	0.01	0.01	Tr	Tr	Tr	Tr	0.02	0.04
Al_2O_3	–	–	0.13	–	–	–	–	0.13	0.40
Fe_2O_3	0.20	0.23	0.25	0.10	0.12	0.08	0.12	0.17	0.40
MnO	Tr	Tr	0.02	Tr	Tr	Tr	0.02	0.02	0.11
MgO	1.48	0.88	5.10	0.18	0.05	0.09	0.16	0.60	0.88
CaO	0.37	4.27	20.40	0.23	0.07	0.07	6.16	54.52	75.85
Na_2O	0.14	0.08	0.15	0.05	0.03	0.04	0.04	0.02	0.02
K_2O	0.04	0.03	0.03	0.03	0.02	0.02	0.02	0.04	0.06
P_2O_5	Tr	0.02	0.01	Tr	Tr	Tr	Tr	0.03	0.04

Table 2

Sample	Spectrum	Lithotype	Wt%						
			O	C	Si	Ca	Al	Mg	Fe
ES-1	1	Oncoid filament	50.0	18.6	25.6	–	1.0	4.8	–
	2	Oncoid filament	34.4	48.5	13.7	–	0.9	2.1	–
S5-20	3	Cells and filaments	51.5	12.3	34.8	–	1.4	–	–
	4	Algal filaments	52.5	17.9	22.2	–	2.1	2.2	2.1
H3-1	5	Stromatolite	42.5	27.6	20.5	5.6	3.2	0.5	–

Table 3

Sample	Description	Mineral phases	Wt%			
			Quartz	Moganite	Calcite	Dolomite
1	Bedded chert and pseudomorphs after gypsum	Quartz, moganite, calcite	77.5	20.7	1.8	–
2	Chert replacing poikilotopic gypsum cementing bioclastic limestone	Quartz, moganite, calcite, dolomite	72.4	21.6	4.9	1.1
3	Associated stromatolites	Dolomite, gypsum, calcite, quartz, ?moganite	–	–	–	–

Figures

Fig. 01

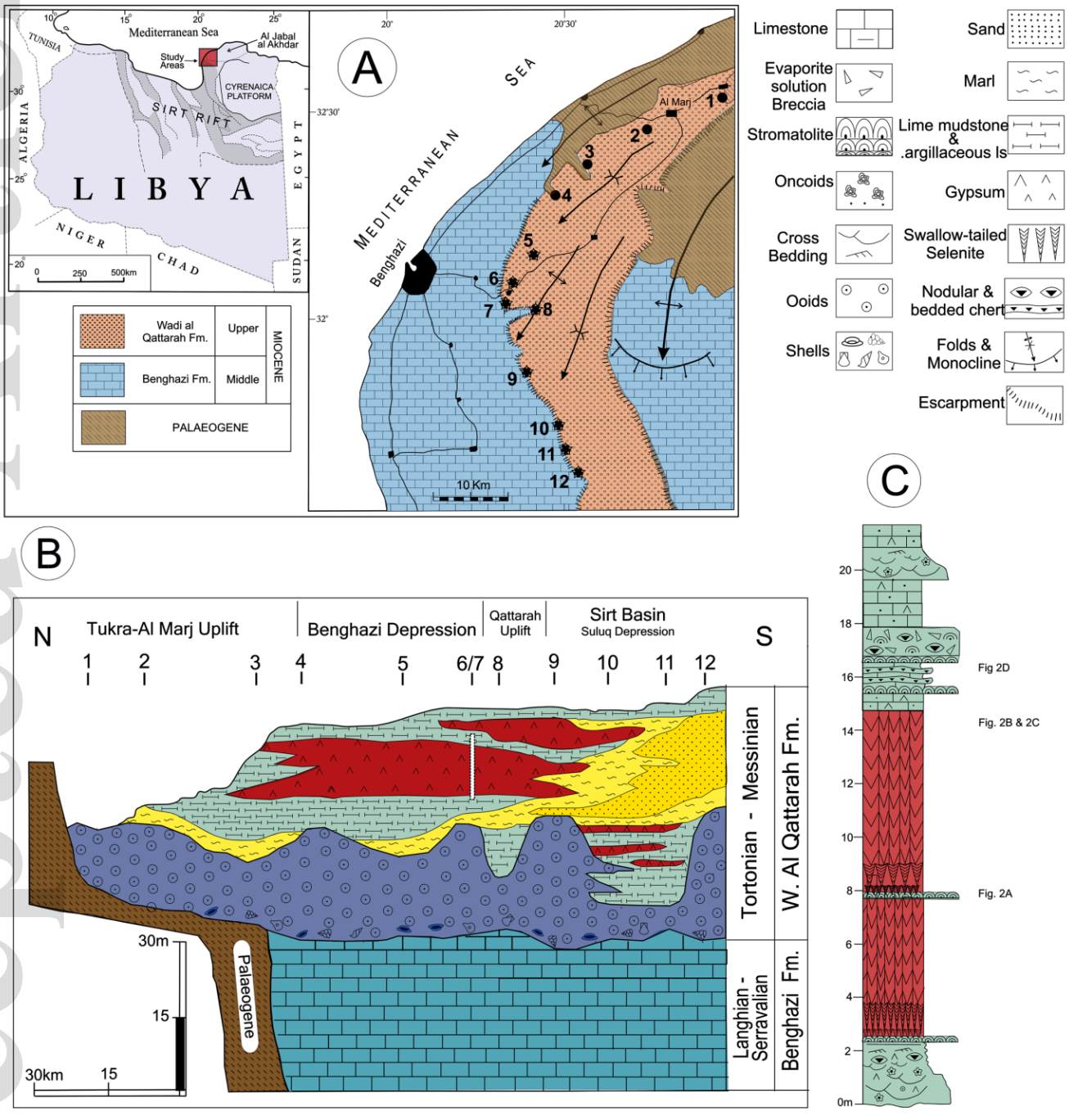

Fig.02

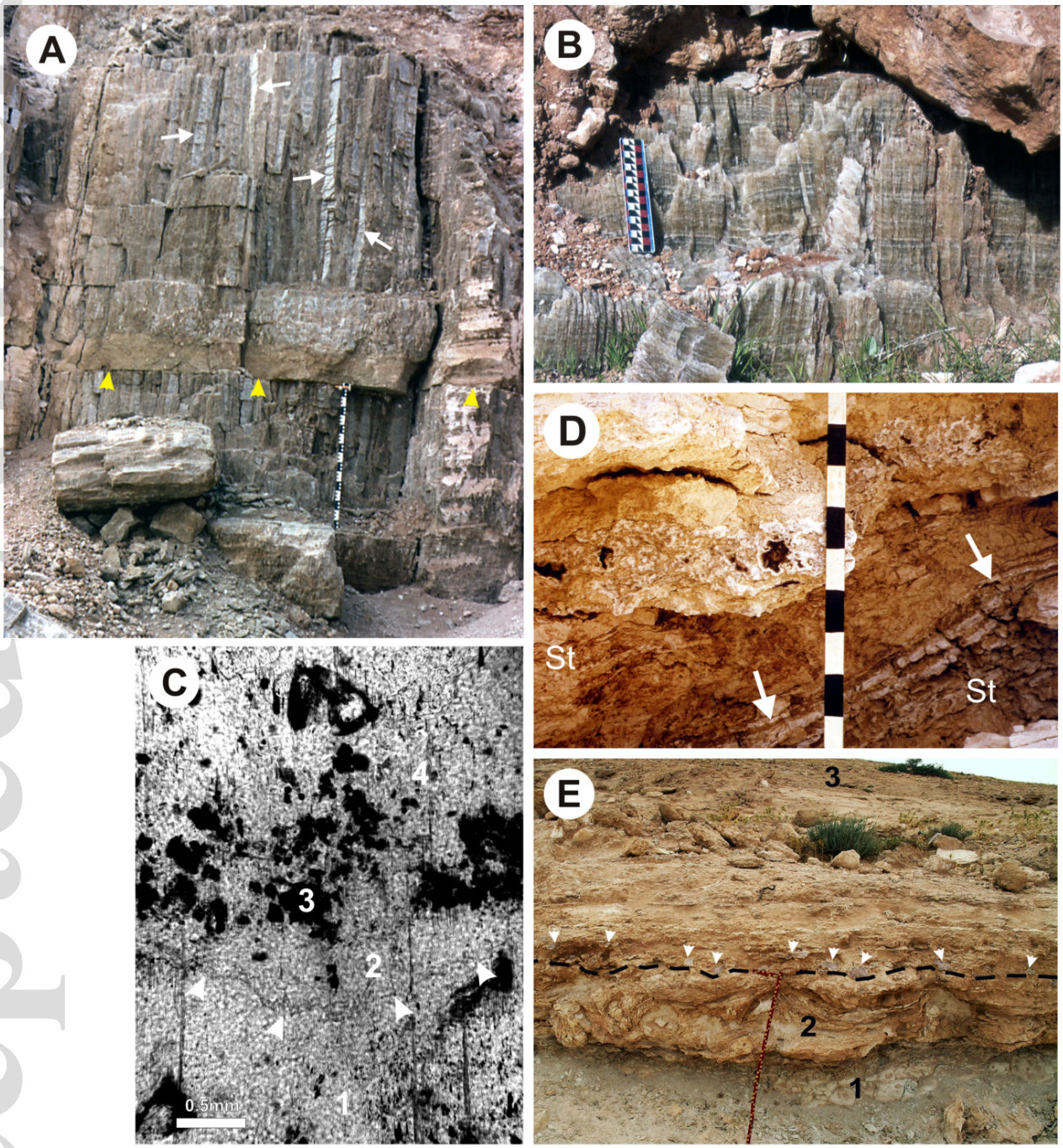

Fig. 03

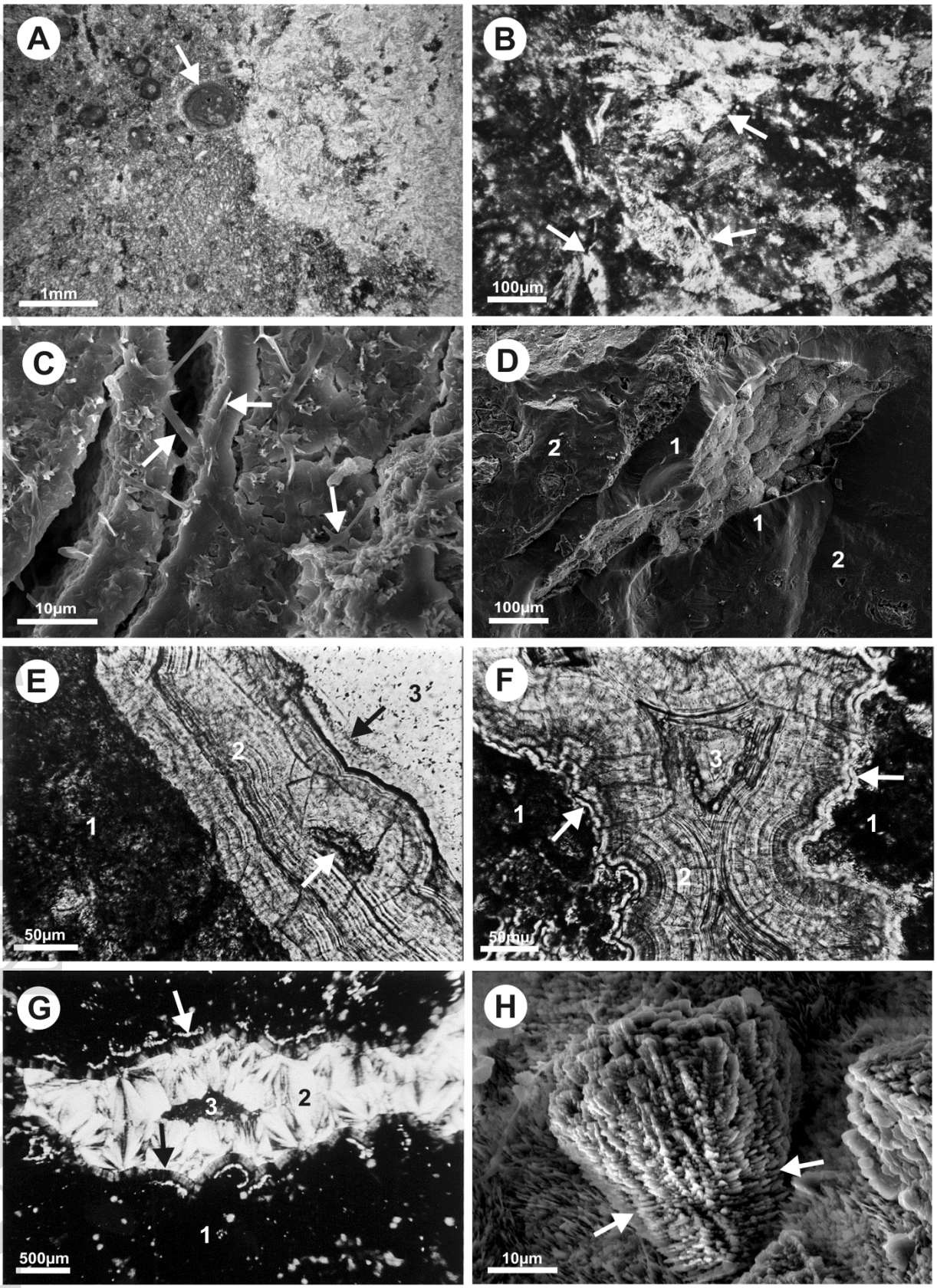

Fig.04

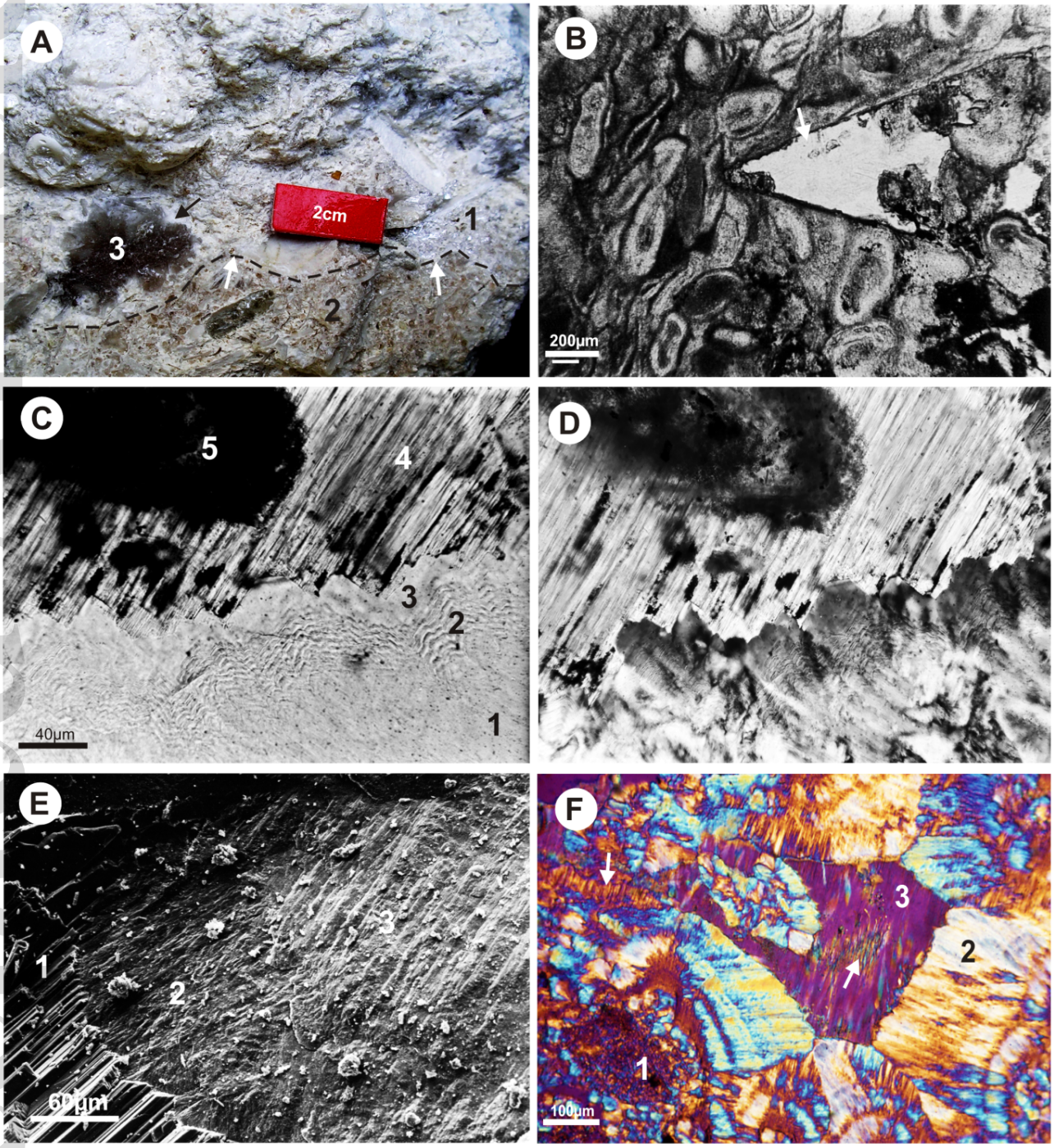

Fig. 05

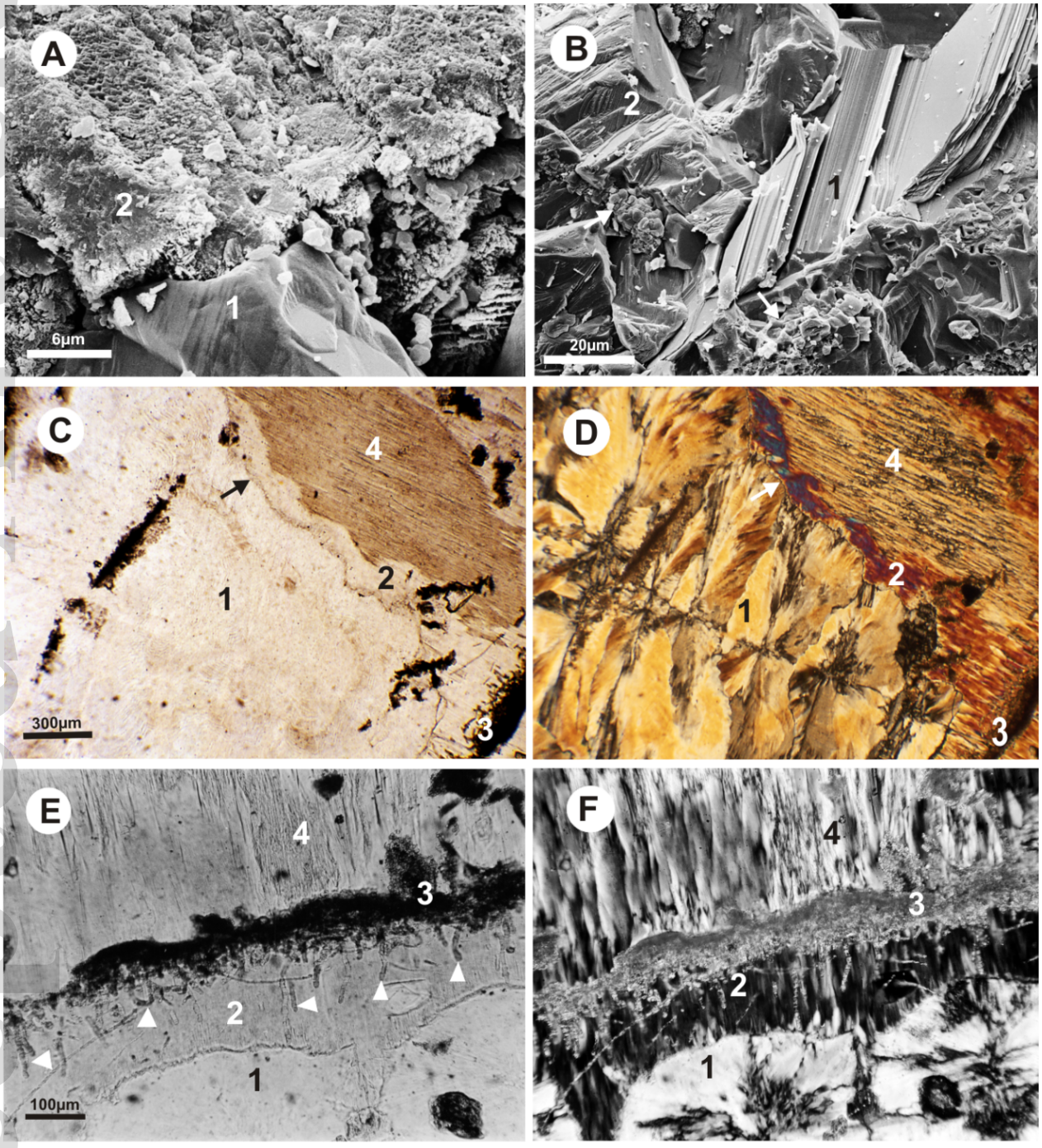

Fig.06

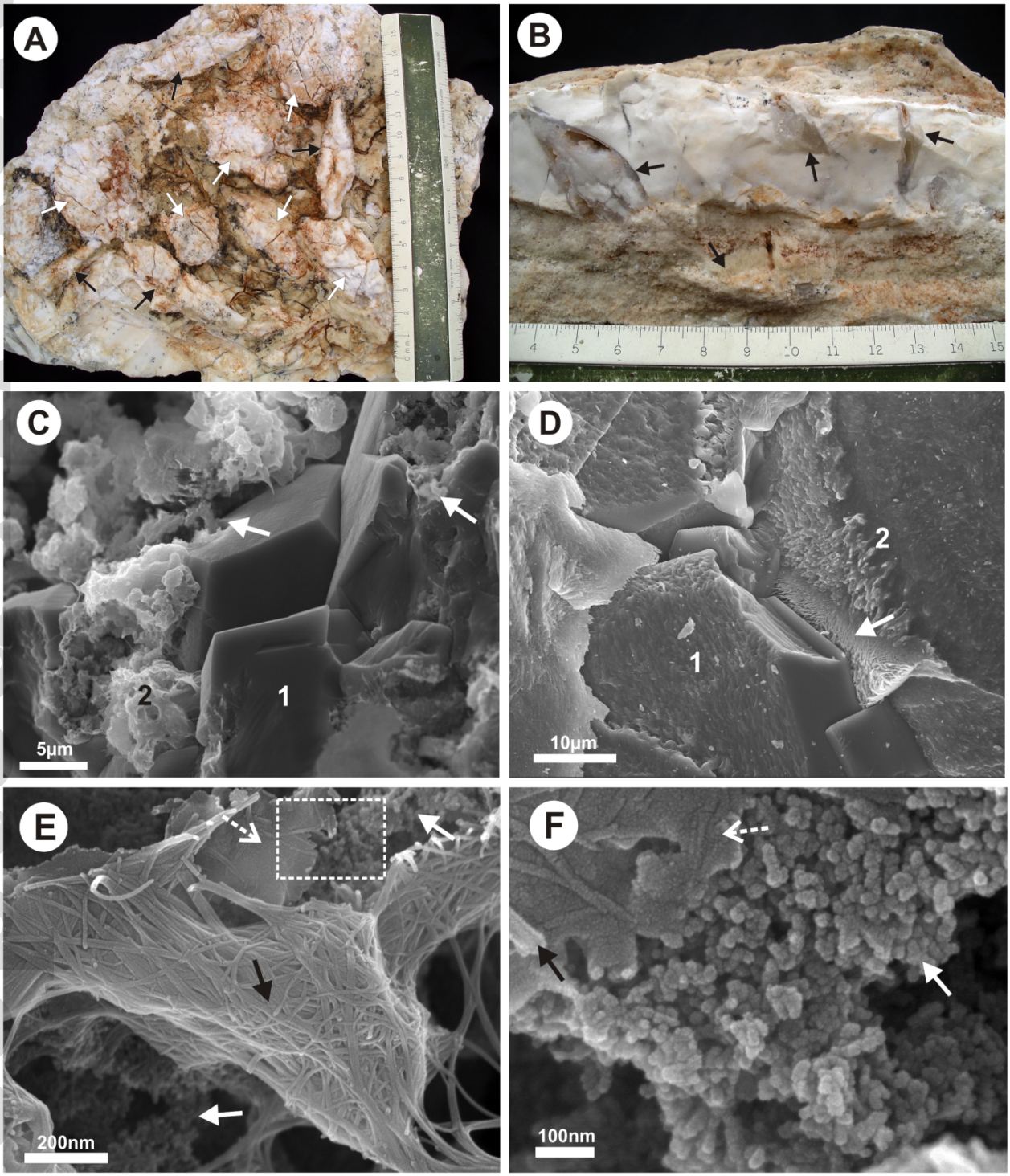

Fig. 07

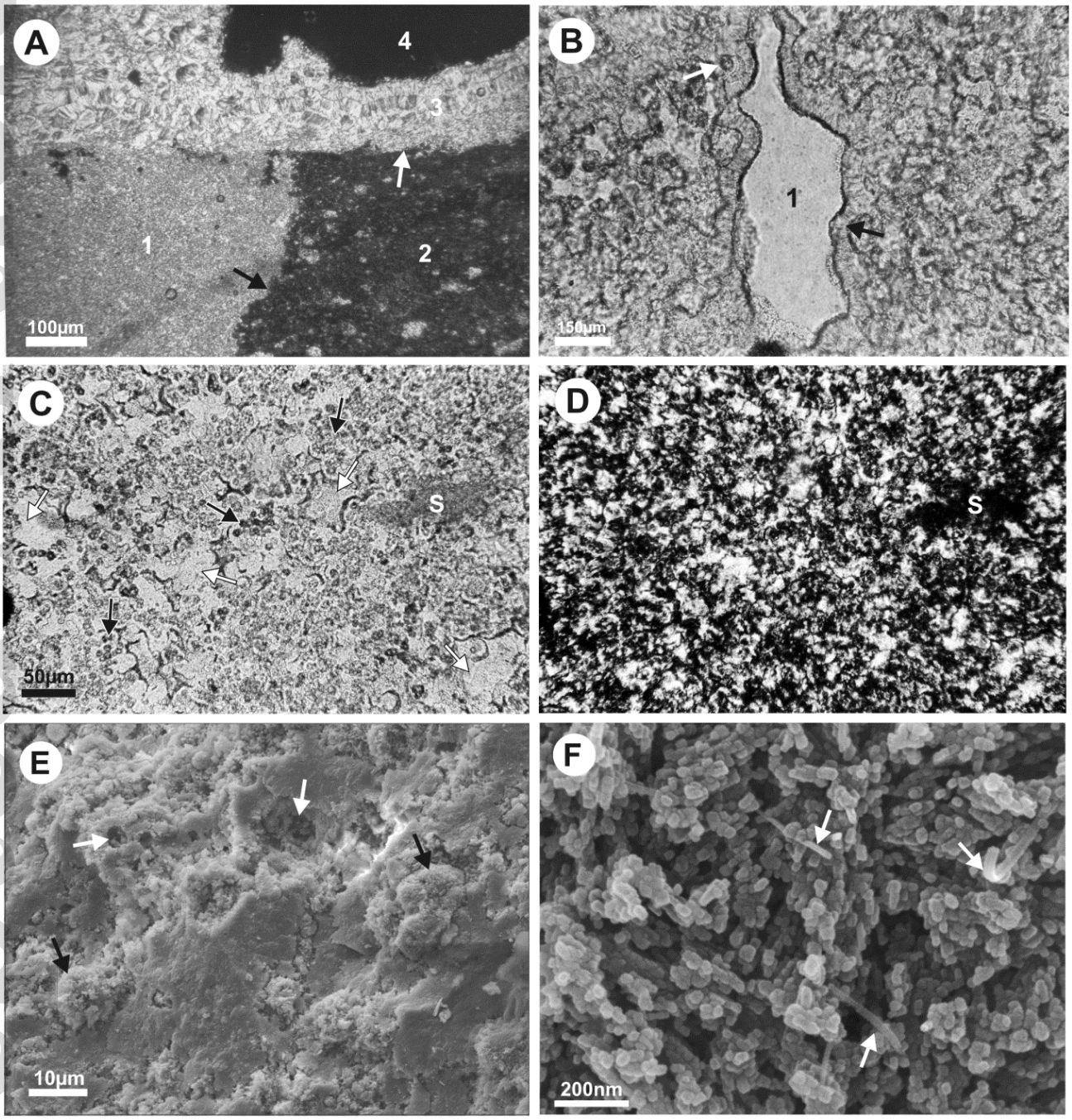

Fig. 08

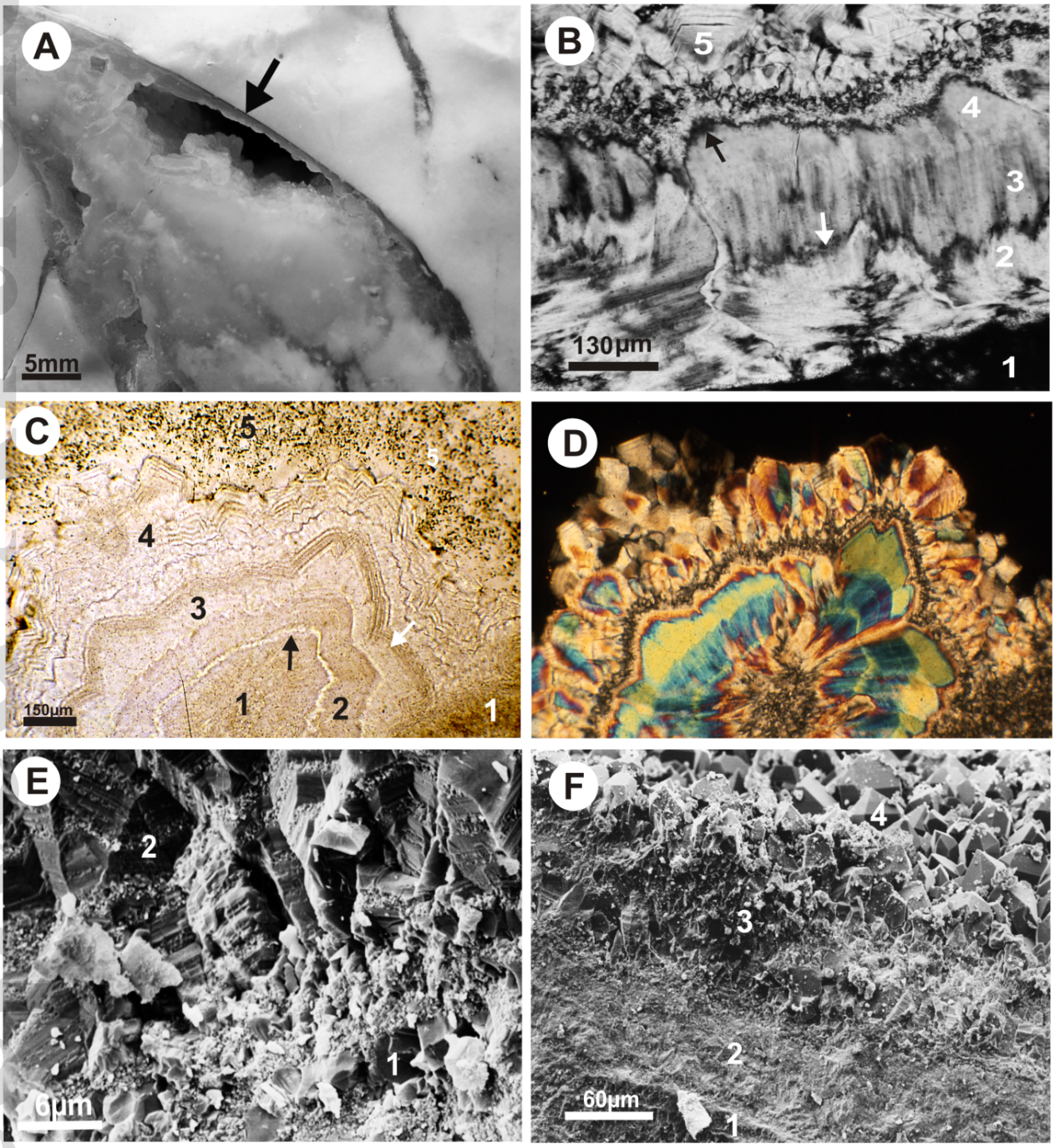

Fig. 09

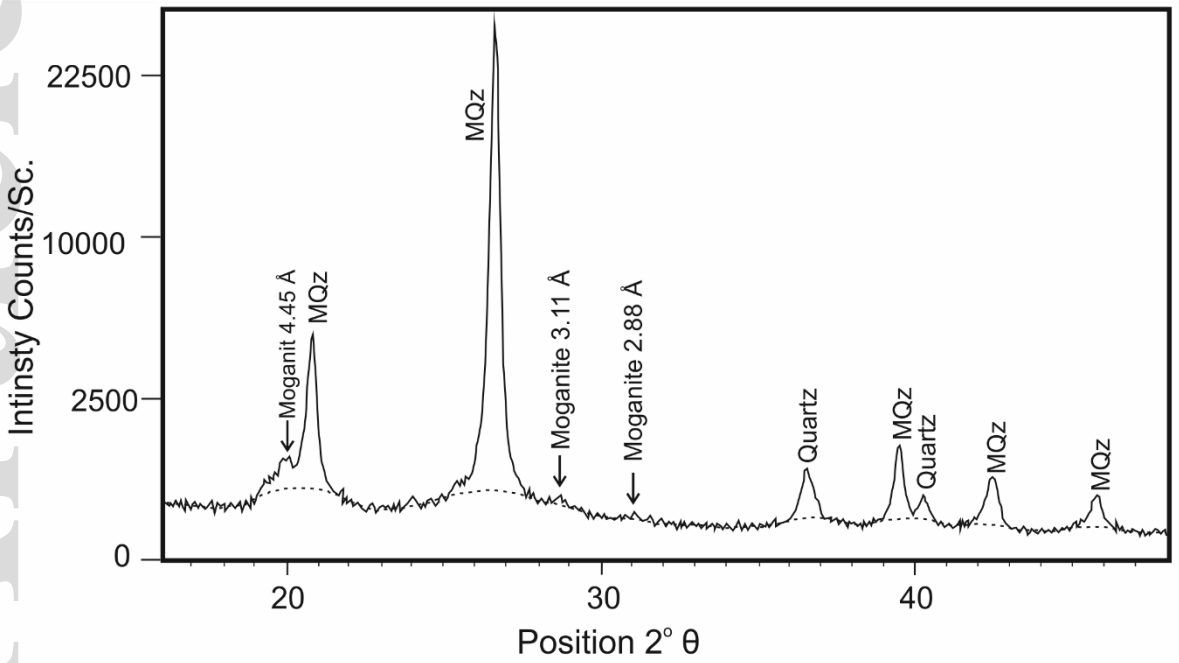

Fig. 10

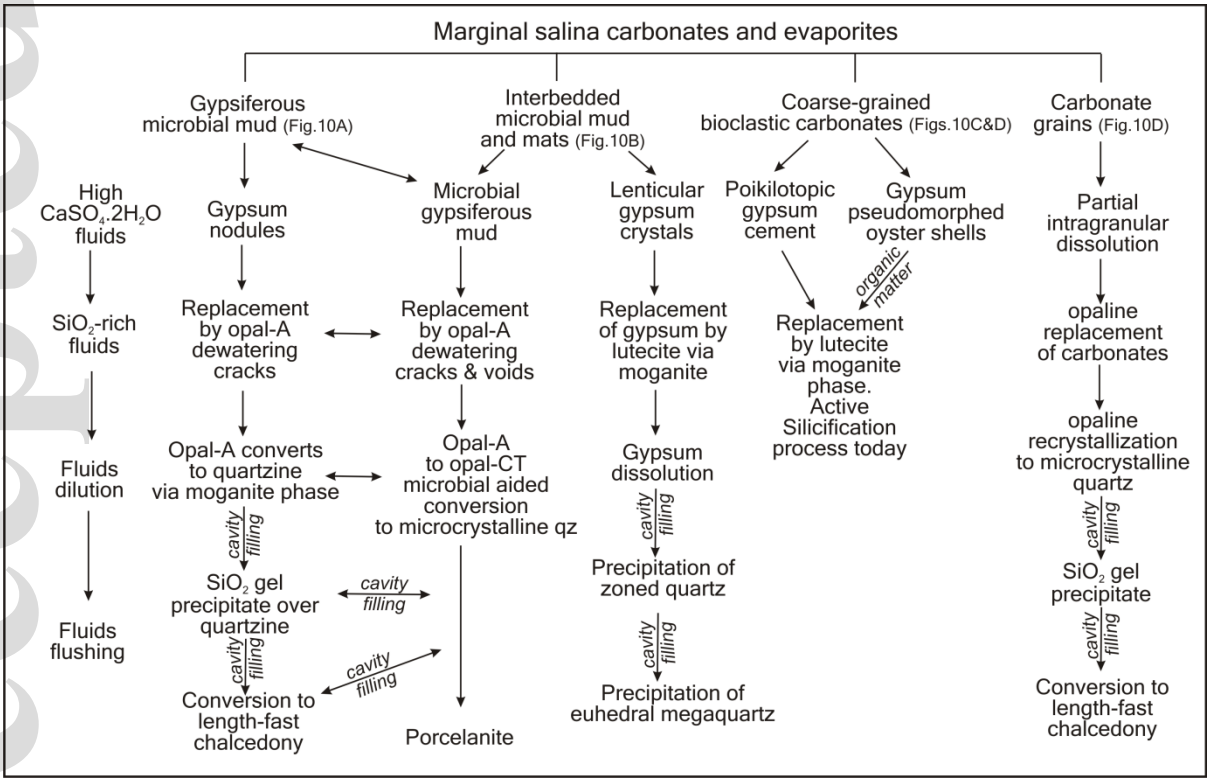

Fig. 11